NAVAL POSTGRADUATE SCHOOL

MONTEREY, CALIFORNIA

THESIS

3D DISCRETE ELEMENT SIMULATIONS OF ACOUSTIC DISPERSION IN SEDIMENTS

by

So Bing Phua

March 2023

Thesis Advisor: Derek Olson
Co-Advisor: Abram H. Clark IV

THIS PAGE INTENTIONALLY LEFT BLANK

REPORT DOCUMENTATION PAGE	*Form Approved OMB No. 0704-0188*

1. AGENCY USE ONLY ***(Leave blank)***	**2. REPORT DATE** March 2023	**3. REPORT TYPE AND DATES COVERED** Master's thesis

4. TITLE AND SUBTITLE 3D DISCRETE ELEMENT SIMULATIONS OF ACOUSTIC DISPERSION IN SEDIMENTS	**5. FUNDING NUMBERS**
6. AUTHOR(S) So Bing Phua	
7. PERFORMING ORGANIZATION NAME(S) AND ADDRESS(ES) Naval Postgraduate School Monterey, CA 93943-5000	**8. PERFORMING ORGANIZATION REPORT NUMBER**
9. SPONSORING / MONITORING AGENCY NAME(S) AND ADDRESS(ES) N/A	**10. SPONSORING / MONITORING AGENCY REPORT NUMBER**

11. SUPPLEMENTARY NOTES The views expressed in this thesis are those of the author and do not reflect the official policy or position of the Department of Defense or the U.S. Government.

12a. DISTRIBUTION / AVAILABILITY STATEMENT Approved for public release. Distribution is unlimited.	**12b. DISTRIBUTION CODE** A

13. ABSTRACT (maximum 200 words)

Sound speed dispersion and frequency dependence of attenuation in marine sediments are important for any undersea activities using acoustics, such as remote sensing and target detection. Current established models use grain shearing and fluid viscosity as the source of loss in sediments, both of which may not be significant given the relatively small strains imposed by most acoustics' signals. In this paper, we analyze a source of attenuation due to compressional losses in grains, modeled with a dashpot term. Discrete element modelling (DEM) using Large Scale Atomic Molecular Massively Parallel Simulator (LAMMPS) was used to model motions of distinct particles in the system. A small amplitude pressure wave was introduced into the channel via an oscillating boundary wall and its effect on each discrete particle was measured to obtain the sound speed and attenuation coefficient. The measurements with sets of varying frequencies for system size of up to 50000 particles exhibit similar relationships with experimental data used for comparison in this paper. In particular, we were able to recover the observed frequency dependence of attenuation, following a power law of frequency squared at low frequencies and the square root of frequency at high frequencies for all system sizes used in our analysis. The small number of parameters used in our theory present a much more tractable and parsimonious problem for geo-acoustic inversion than the more complicated established models.

14. SUBJECT TERMS discrete element simulation, discrete element modelling, DEM, compression losses, Large Scale Atomic Molecular Massively Parallel Simulator, LAMMPS, frequency dependence attenuation, sediment acoustics, sound speed dispersion, consistent power law, grain to grain contacts	**15. NUMBER OF PAGES** 91
	16. PRICE CODE

17. SECURITY CLASSIFICATION OF REPORT Unclassified	**18. SECURITY CLASSIFICATION OF THIS PAGE** Unclassified	**19. SECURITY CLASSIFICATION OF ABSTRACT** Unclassified	**20. LIMITATION OF ABSTRACT** UU

NSN 7540-01-280-5500

Standard Form 298 (Rev. 2-89)
Prescribed by ANSI Std. 239-18

THIS PAGE INTENTIONALLY LEFT BLANK

3D DISCRETE ELEMENT SIMULATIONS OF ACOUSTIC DISPERSION IN SEDIMENTS

So Bing Phua
Major, Republic of Singapore Navy
BME, Nanyang Technological University , 2014

Submitted in partial fulfillment of the
requirements for the degree of

MASTER OF SCIENCE IN PHYSICAL OCEANOGRAPHY

from the

NAVAL POSTGRADUATE SCHOOL
March 2023

Approved by: Derek Olson
Advisor

Abram H. Clark IV
Co-Advisor

Peter C. Chu
Chair, Department of Oceanography

THIS PAGE INTENTIONALLY LEFT BLANK

ABSTRACT

Sound speed dispersion and frequency dependence of attenuation in marine sediments are important for any undersea activities using acoustics, such as remote sensing and target detection. Current established models use grain shearing and fluid viscosity as the source of loss in sediments, both of which may not be significant given the relatively small strains imposed by most acoustics' signals. In this paper, we analyze a source of attenuation due to compressional losses in grains, modeled with a dashpot term. Discrete element modelling (DEM) using Large Scale Atomic Molecular Massively Parallel Simulator (LAMMPS) was used to model motions of distinct particles in the system. A small amplitude pressure wave was introduced into the channel via an oscillating boundary wall and its effect on each discrete particle was measured to obtain the sound speed and attenuation coefficient. The measurements with sets of varying frequencies for system size of up to 50000 particles exhibit similar relationships with experimental data used for comparison in this paper. In particular, we were able to recover the observed frequency dependence of attenuation, following a power law of frequency squared at low frequencies and the square root of frequency at high frequencies for all system sizes used in our analysis. The small number of parameters used in our theory present a much more tractable and parsimonious problem for geo-acoustic inversion than the more complicated established models.

THIS PAGE INTENTIONALLY LEFT BLANK

Table of Contents

List of Figures

List of Tables

THIS PAGE INTENTIONALLY LEFT BLANK

List of Acronyms and Abbreviations

ASW	Anti-Submarine Warfare
BICSQS	Biot-Stoll plus Contact Squirt Flow and Shear
DEM	Discrete Element Modelling
HPC	High Performance Computing
LAMMPS	Large Scale Atomic Molecular Massively Parallel Simulator
NPS	Naval Postgraduate School
VGS	Viscous Grain Shearing

THIS PAGE INTENTIONALLY LEFT BLANK

Acknowledgments

I would like to thank Derek Olson for his patience and assistance in helping me understand the research topic as well as editing my paper. Most of all, thanks to Abe Clark, who has spent the past year helping me with LAMMPS, MATLAB and guiding me to the conclusion of this research.

I would also like to thank the Oceanography Department and the Undersea Warfare Department of Naval Postgraduate School for the amazing support given during my time here.

THIS PAGE INTENTIONALLY LEFT BLANK

CHAPTER 1:
Introduction

1.1 Background

An acoustic signal involves forces travelling through some medium, such as the ocean environment. As the sound wave propagates through the medium, it loses energy, which is manifested as attenuation, which typically depends on frequency. This is an exponential decrease in acoustics intensity as a function of spatial position. Signal propagation through the ocean is dependent on the frequency of the wave, a characteristic sound speed of the medium, as well as other factors like sea surface roughness, marine biologics and composition of seabed bottom [1]. In particular, the effect of signal attenuation for acoustic waves propagating in the seafloor plays an important role in many naval applications such as mine warfare and anti-submarine warfare. As such, research and development efforts in studying the acoustic properties of marine sediments have gained much traction in the past three decades for both commercial and military uses.

Attenuation is the combined effects of scattering and absorption. In this paper, we will only focus on attenuation due to absorption. The rate of exponential decay is the attenuation parameter, α, as described in $I(x) = I_o e^{-2\alpha x}$. Militarily, understanding attenuation plays an paramount role in navy's target detection operations and even hydrography or surveying efforts. In particular, for mine warfare operations, detection and classification of underwater contacts with sonar imagery has always been a challenge for the navy. Its operating environment such as attenuation of signal within the water columns and from sea-floor interactions will directly impact the ability to detect and classify mines. A good grasp of signal attenuation effects from marine sediments will allow for better prediction and sense making of sonar imagery that improve target detection success rate. In ASW, attenuation affects the level or intensity of signal received by receiver, that directly affect its ability to track adversaries submarine. Other challenges includes weapon systems that uses acoustics technology to track and lock on target. Henceforth, by understanding the attenuation behavior of an operating environment allowed war fighters to set appropriate target detection threshold.

Marine sediments types ranges from fine muds to coarse sands and rocks, and in most instances combination of thereof. The physical properties such as grain size, density, porosity, composition and roughness may all play some role in the wave speed and the rate of signal attenuation. This attenuation also varies based on the sea floor layers and gradients [2]. Seafloor properties vary spatially due to underwater currents and presence of marine biologics. In order to better predict acoustic propagation, researchers have developed seabed geo-acoustic models to predict signal losses in different ocean environment. These models will greatly aid scientists and engineers in developing state of art undersea technology with increased range in undersea communications, target detection ability, undersea navigation technologies and many others. However, predicting acoustics propagation in marine sediment have been challenging due to theoretical and experimental limitation in this field which inevitably led to varying theories and results in this field. A set of field experiments and measurements data in Figure [3] show trends of f^2 at low frequency and $f^{\frac{1}{2}}$ at high frequency for attenuation. Additionally, constant sound speed was observed at low frequency with increasing sound speed ratio at high frequency. This set of experimental data will be used extensively in this paper.

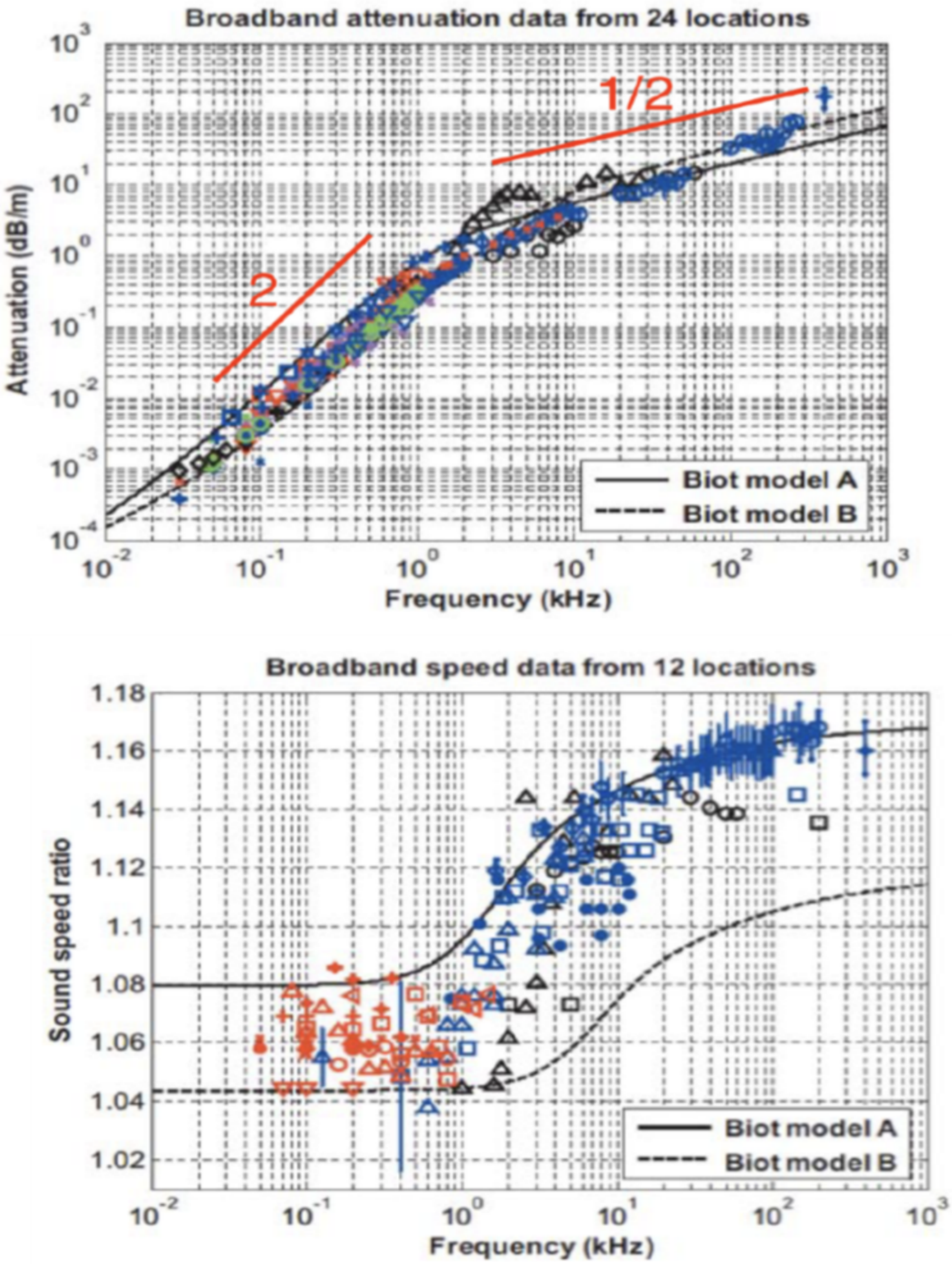

Figure 1.1. Field experiment and measurement datasets for attenuation coefficient and sound speed ratio. Source: [3]

1.2 Current Models

With significant effort invested in creating seabed geo-acoustics models, several well-known models are created to explain and quantify the attenuation. Fundamentally, sediment acoustics involves propagation through a water-saturated dense packing of grains (i.e., sand or silt). Although a host of other factors (as mentioned above) may play a role, it is useful to consider this simplified picture to understand the main physics. Thus, current theories focus on some physical mechanism included in such a simplified system. The Biot-Stoll [4]–[6] theory focuses on the porous nature of marine sediments and attributed the attenuation losses as a result of viscous damping of waves in the pores. Acoustic waves travel through the porous nature of sediment akin to a "Swiss cheese" and creates an interaction between relative motion of pore fluid with the sediment structure that leads to attenuation losses. Biot-Stoll model predicts a non-linear relationship between attenuation and frequency as well as exhibits a strong non-linear dispersion of sound speed. Their theories are able to fit to experimental data in Figure 1.1 with $\alpha(f)$ proportional to f^2 for $f < 1kHz$ at low frequency and $f^{\frac{1}{2}}$ for $f < 10kHz$. However, this model is highly dependent on a large number of fit parameters that are challenging to measure or predict due to ocean dynamics and its variability. Physically, some of these parameters, we predict are unlikely to play an important role given the small strain amplitudes in acoustics propagation. Furthermore, Biot-Stoll's model are fundamentally poroelastic instead of granular since it focuses on energy dissipation of stress induced viscous flow.

The other commonly used model is Buckingham's grain shearing (GS) [7], [8] model that considers the frictional slips attributed from grain to grain contact in marine sediments as the key influence on attenuation of wave signals as shown in Figure 1.2. This is done by adding a frequency-dependent damping term, which is inspired by inter-granular stick-slip motion, to the wave equation without taking into consideration the viscosity of pore fluid since they treated their medium as homogeneous continuum. Recent works in the GS theory starts to expand their works to include the effects of viscosity of pore fluid on a granular structure/layers, otherwise termed as the VGS model [9]. This new model predicts similar results with Biot-Stoll in sound speed dispersion and frequency dependence of sound attenuation at lower frequency. At high frequency, its sound speed dispersion curves are similar to those of GS model that does not correspond well with experimental results. Other models were also derived to build on the incompleteness or inaccuracy of Biot-Stoll and

Buckingham model whereby experimental data shows a significantly higher sound speed dispersion than in Biot-Stoll and inaccuracy of attenuation frequency dependency at high frequency for Buckingham model. Chotiros and Isakson [10] developed the Biot-Stoll plus contact squirt flow and shear (BICSQS) model that studied both the granular nature of marine sediments (grain to grain contact) as well as the viscous effect that includes squirt flow and shear drag. Their results were more consistent with the measured experimental results [11]. However, their model inherits, if not increases the complexity of Biot-Stoll model as there are more parameters involve in its theory.

While these models are commonly used, there are some questionable applicability in the field of marine sediments. Apart from being complex in nature, Biot-Stoll model originated from Biot model that was built upon limestone and was later expanded to sediments by Stoll [5]. However, sediments do not have a porous structure in the same way as lime stone. Furthermore, his work does not focus on the granular nature of marine sediments which we believed have significant impact on its loss mechanism. While Buckingham VGS model studied that granular nature, his theory attributed the loss mechanism to frictional slips but produced varying results from experimental data. Our model will focus on the granular nature of marine sediments. The primary loss mechanism will be from local, relative motion between grains. Here we will refer to such behavior as compression losses, in that periodic compression between two grains is not energy conserving. This is commonly used in granular physics via a restitution coefficient; in a marine environment, these losses could be amplified by the presence of the fluid.

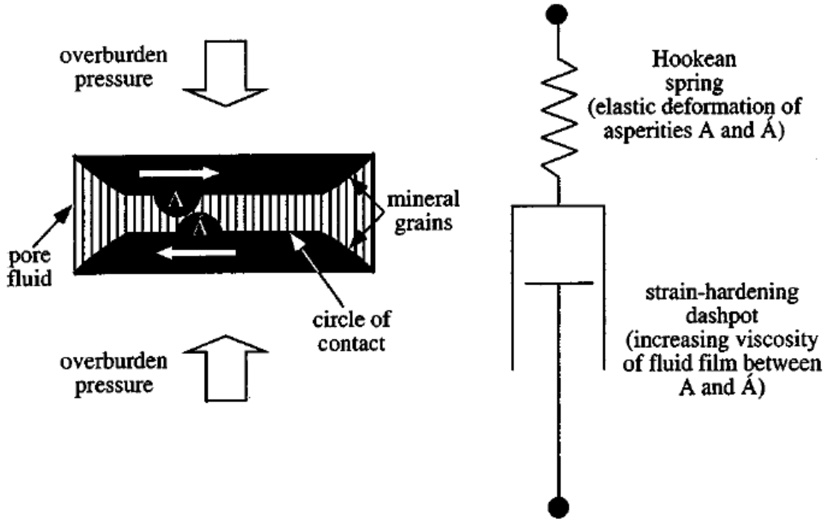

Figure 1.2. Schematics of Buckingham Model. (Left) Shearing of granular material on the circle of contact. (Right) Hookean spring and nonlinear strain hardening dashpot in series. Source: [12]

1.3 Approach

Compression losses are commonly used in the granular physics community but are not included in either of the current models discussed above. We will show that focusing on this loss mechanism could lead to a vastly simplified theory of acoustic propagation in marine sediments that is deeply connected to their granular nature. This model is broadly similar to the grain shearing model because it is fundamentally granular. Unlike the Buckingham model, which attributed the key loss mechanism to the effect of frictional slips between granular surface, our approach is to study the effects of plastic or viscous-like losses during normal compression at grain-to-grain contacts. In particular, the plastic losses have been neglected by both Biot-Stoll and Buckingham models. The Biot-Stoll model typically assumes that the frame losses are zero, hence neglecting the effect of inter-particle interactions.

In essence, granular materials can be regarded as a disordered network of discrete elements, interlinked by contacts that involve elastic and dissipative effects. Forces are known to be transmitted inhomogeneously, where the structures involving stronger forces are often called "force chains." These are quasi-1D structures, although they branch and rejoin in complex patterns [13].

Thus, some aspects of sediment acoustics can be understood using a one-dimensional (1D) picture where forces acting on each granular structure can be regarded as a "spring mass system". In such system, the particles in contact will interact with their neighbors via repulsive springs, capturing repulsive contact forces, and viscous-like dash-pots, capturing inelastic effects from plastic deformations at contacts. When forces propagating along such a 1D chain, or along force chains in a granular packing, short wavelengths will involve more relative motion at contacts than long wavelengths. Hence this model has intrinsic frequency dependence of attenuation.

Our central hypothesis is that the dominant mechanism attributing to frequency dependent attenuation is energy dissipation at grain to grain contacts. In dry granular materials, energy is lost during compression due to the effects of "plastic rearrangement." This is a non-reversible process whereby the poly-crystalline structure changes as grains undergo small deformation. In the granular physics and engineering communities, this is commonly modeled by a damping term that depends linearly on the relative velocity between grains [14], [15]. In application to marine sediments, such linear term could also be expanded to include the viscous effects from the presence of a fluid, if needed.

The primary goal of this thesis is to develop and validate a simulation framework for studying acoustic propagation in three dimensional granular packings. We will begin by studying frictionless spheres with no explicit fluid, but with a dashpot term included at each grain-grain contact to model compression losses. Future work will add additional terms as needed, in order to disentangle the role of each. We use Discrete Element Modeling (DEM) software called Large Scale Atomic Molecular Massively Parallel Simulator (LAMMPS) to solve the large system of equations that is required to model grains interactions. If our central hypothesis has merit, then these results should correlate well with experimental data shown in Figure 1.1 with the correct power law behavior. We indeed find good preliminary agreement between our 3D results using frictionless grains, including only repulsive and dashpot forces, suggesting that our approach is valid. We test that this model is independent of the system size. Lastly, we study the effects of shear waves in our simulation model understanding that waves are characterized in two forms, transverse and longitudinal. We find that, even for frictionless spheres, shear waves propagate with behavior similar to compression waves. Our theory could vastly simplify the theoretical framework used to describe and predict the acoustical properties of marine sediment by reducing the number of fit parameters to just a single fit parameter (the material's restitution coefficient) based on its granular nature. The small number of parameters used in our modeling present a much more tractable problem for geo-acoustics inversion.

In the next chapter, we will provide details on the contact law mechanics where we relate granular physics to sediment acoustics and eventually provide explanations on how we derive at our 1D theory. The simulation methodology is detailed in Chapter 3 with results and discussions in Chapter 4. We then provide a conclusion for the paper in Chapter 5.

CHAPTER 2:
Theory

2.1 Contact Laws

As stated at the end of the previous chapter, our goal is to explore the hypothesis that the dominant mechanism attributing to similar dispersion relations as per experimental data shown in Figure 1.1 is the energy dissipation at grain to grain due to normal force, which could arise from plastic rearrangements inside grains and could be amplified by the fluid. Specifically, the goal of this thesis is to develop a 3D simulation framework that can model this situation. This chapter describes a simplified model for grain-grain interactions that include a repulsive term as well as a dissipative force component. We describe the interaction rules that will be used in both theoretical and simulation investigations.

2.1.1 Quantities Associated with Inter-Particle Contacts

The effects of two contacting solid particles can be described by force-displacement laws in both normal and tangential directions as shown in Figure 2.1. Simplified geometries (e.g., spheres) with the assumptions of non-cohesive and dry grains will restrict the interactions to six degrees of freedom (three translational and three rotational). When two particles are in contact, it causes a virtual overlap, modeling a physical deformation that would occur between two physical particles.

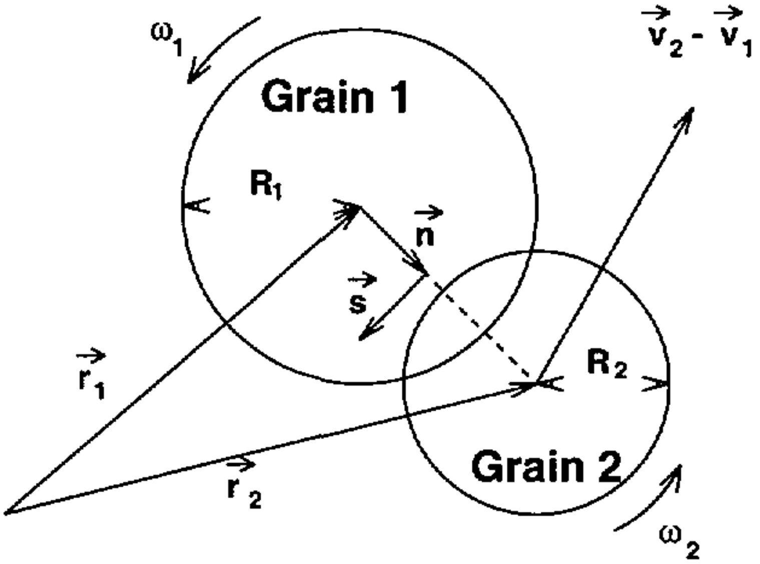

Figure 2.1. Quantities involved in a general contact between two grains. Source: [16]

The deformation, represented by the overlap in Figure 2.1 is typically represented by δ in equation (2.1) as described by [17]:

$$\delta = \max(0, R_1 + R_2 - |r_2 - r_1|) \tag{2.1}$$

Unit vectors, n and s are used to differentiate the forces and velocities in normal and shear components respectively as described by [17] are shown in equation (2.2) and (2.3)

$$n = \frac{r_2 - r_1}{|r_2 - r_1|} = (n_x, n_y) \tag{2.2}$$

$$s = (n_y, -n_x) \tag{2.3}$$

2.1.2 Normal Compression

The simplest way to model the force effects of contacts between two spheres is by using two terms: a linear restoring force and a dissipation force as shown in equation (2.4)

$$F_n = -\kappa\delta - \gamma\dot{\delta} \tag{2.4}$$

where κ is the effective spring constant, γ is the magnitude of dash-pot like force, and $\dot{\delta}$ represent the time derivatives of displacement (overlap). The dashpot term is the simplest way to model dissipation at grain-grain contacts. In dry granular materials, energy dissipation from normal contacts appears in three forms, namely plastic deformation, visco-elasticity of material and elastic waves (inside individual grains) excited by the compression. Elastic waves are always present but often neglected due to its small energy dissipation. Nevertheless, the dash-pot is meant to model some combination of these three effects.

The value of the dashpot can be fit to data, as shown by the theory below. However, in dry granular media, it can be connected to physical parameters via the restitution coefficient, $\mathrm{e_n}$, which is a measure of kinetic energy loss after two objects collide. Note that this is typically used in a kinetic situation, whereas our grains are in persistent contact. The values of e_n range between 0 to 1 whereby lesser energy is lost when its restitution coefficient in high (i.e., closer to 1). The primary loss mechanism from the collision is dependent on the material of the objects, the speed of the collision, and possibly other parameters, but can be approximated as a constant over wide ranges. e_n is defined as a ratio of the final velocity to its initial velocity between two objects as shown in equation (2.5) where superscript f refers to final and superscript i refers to initial [16].

$$e_n = -\frac{v_n^f}{v_n^i} \tag{2.5}$$

The physical bounds of γ are often controlled by the value of e_n given by

$$e_n = \exp\left(-\frac{\gamma}{2m_{\mathrm{eff}}}t_n\right) \tag{2.6}$$

where $m_{\mathrm{eff}} = (m_1 m_2)/(m_1 + m_2)$ and t_n denotes the duration of collision. Physically, the value of e_n will affect the magnitude of γ, but this connection assumes a kinetic, collisional picture for the granular system, whereas our system involves grains in persistent contact.

In order to study the frequency dependence on such a system, we simply assumed a constant value of the dashpot, i.e., a constant value for γ. Our theory will focus on effects of different wavelengths resulting from different frequencies on the inter-particle forces. Understanding that the wavelength of sound are much greater than inter-atomic spacing, we can take the long wave-length limit and this will yield a wave equation that includes a dissipative term.

2.1.3 Hertzian Contact Theory

In equation (2.4), we used a linear spring to model the restoring force between inter-particle contacts. Hence in this section, we will justify the use of linear spring in our theory using hertzian contact theory. Acoustics properties of granular materials are generally characterized by properties of the solid frame, pore fluid (if present) and the fluid/frame interactions [6]. In most theories, the solid frame properties are typically specified prior for simplification. One of such model is to assume a solid frame made up of individual solid grains of same material in contact whereby the grains are generally assumed to be elastic spheres. The responses of these grains to purely compressive loading are described by the Hertzian contact theory that allows for prediction of the resulting contact area, contact pressure, surface deformation and induced stress on the solids as illustrated in Figure 2.2.

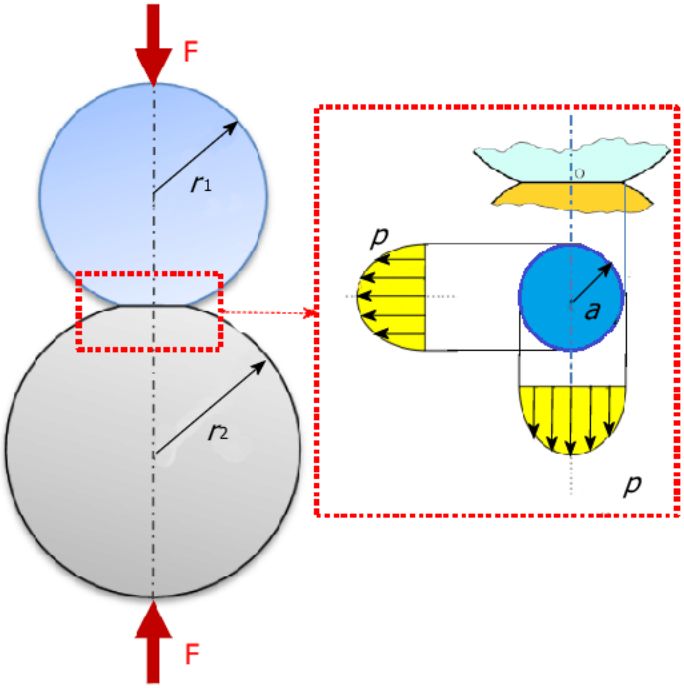

Figure 2.2. Hertzian contact theory, (Left) Two solid spheres in contact by force, F. (Right) Contact stress distribution across hemispherical contact zone of diameter 2a. Source: [18]

Mathematically, Hertzian contact theory is derived from analytical solution of elasticity theory [19] using half space approximation with the following assumptions;

- Surfaces are infinitely large half spaces
- Pressure profiles are parabolic
- Strains are small
- Solids are elastic
- Surfaces are frictionless

These assumptions imply that $a \ll R_{\text{eff}}$ where a is the contact radius and R_{eff} is the effective radius of curvature of two solids. In most instance, the contact force f between the two spherical spheres can be written in the form of $f \propto \delta^{\beta}$ where δ again is the deformation of each sphere while β is dependent on the geometry of particle with $\beta = \frac{3}{2}$ for spheres. Contact area, α is given by $\alpha \propto f^{\frac{1}{\beta}}$ for circular contact as shown on the right of Figure 2.2. Sound velocity c is governed by stiffness of the contacts κ represented by a spring-mass system as illustrated in earlier section where $\kappa = \frac{df}{d\delta}$. In experimental 1D model, the relationship between c and κ was found to be $c \propto \sqrt{\kappa}$ for a variety of materials [20].

The prediction of particle responses in Hertzian contact theory underlies model of wave propagation. When propagating forces are small compared to the preexisting forces, then each nonlinear spring can be approximated as a linear spring with value κ. With that, it justify the use of linear forces at each spring when assuming that the propagating signals are small. Nevertheless, we acknowledged that forces in granular media are inherently heterogeneous, resulting in different contact stiffness at each contact. Furthermore, the effects of "no contacts" could also be present when particles contacts separate during the propagation which leads to non-linearity effects. This also means that the bulk modulus is not a homogeneous material property which may produce interesting novel results, which we leave as a topic for future study. With hertzian contact theory, we can predict $c \propto P^{\frac{1}{6}}$ for 2D and 3D systems of spherical particles. To minimize the non-hertzian effects arising from particle asperities and contact rearrangement, value of P must fall above critical P. In this instance, P is defined as the system pressure.

2.2 1D Theory

Marine sediments are in essence a disordered network of discrete elements, consisting of contacts between particles that involve both elastic and dissipative effect as explained earlier. When a mechanical wave travels through a medium, its amplitude decays gradually as it moves further down the channel. A wave travelling through a granular medium involves forces moving along a disordered network of discrete elements. Therefore, we first consider the case of an acoustic signal propagating along a single "force chain" by modeling the granular media as a 1D chain as depicted in Figure 2.3. Waves with shorter wavelengths will involve more relative motion at contacts hence providing a granular mechanism for a frequency-dependent attenuation relationship.

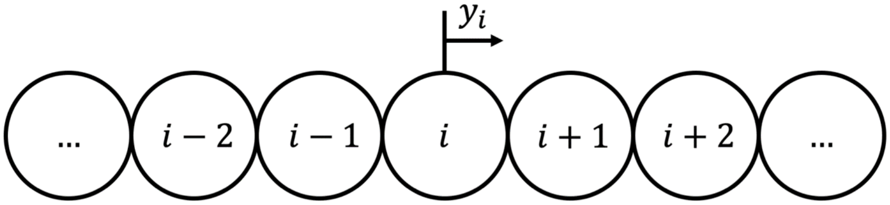

Figure 2.3. 1D granular chain

2.2.1 Wave equation and solutions

The 1D chain can be modeled using a simple linear spring dashpot system as depicted in Figure 2.4 to discuss the interactions between different granular particle. The "virtual overlap" caused by deformation are represent by the displacement y_i as shown resulting in two force components from the neighboring particle. Assuming similar forces between grain i and $i-1$ and using m as the grain mass, the force equation on grain i can be written as

$$m\ddot{y}_i = -\kappa(y_i - y_{i+1}) + k(y_{i-1} - y_i) - \gamma(\dot{y}_i - \dot{y}_{i+1}) + \gamma(\dot{y}_{i-1} - \dot{y}_i) \tag{2.7}$$

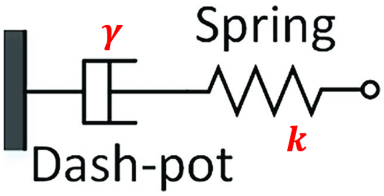

Figure 2.4. Linear spring dash-pot schematics. Adapted from [21]

Assuming that the spacing between discrete sites i and $i+1$ and i and $i-1$ is d, and using the limit definition of a derivative (thus, implicitly assuming that all wavelengths are large compared to a single grain), this will yield a non-linear wave equation in the following form:

$$my_{tt} = \kappa d^2 y_{xx} + \gamma d^2 y_{txx} \tag{2.8}$$

Here, subscripts now denote derivatives and x is the distance along the chain. By guessing a plane wave solution with

$$u(x,t) = e^{i(\tilde{k}x-\omega t)},$$

and defining $\tilde{k} = k + i\alpha$, we get the following solutions for each term in equation 2.8

$$y_{tt} = -\omega^2 y$$

$$y_{xx} = -\tilde{k}^2 y$$

$$y_{txx} = i\omega\tilde{k}^2 y$$

and by substituting it into equation (2.8) and simplifying it, we arrive with

$$m\omega^2 = \tilde{k}^2\kappa d^2 - i\omega\tilde{k}^2\gamma d^2 \tag{2.9}$$

Since $\tilde{k}^2 = -k^2 - \alpha^2 + 2ik\alpha$, this gives us two equations: a real part,

$$m\omega^2 = (k^2 - \alpha^2)\kappa d^2 + 2k\alpha\omega\gamma d^2,$$

and an imaginary part

$$0 = 2k\alpha\kappa d^2 + (\alpha^2 - \kappa^2)\omega\gamma d^2.$$

Defining dimensionless quantities,

$$\hat{k} = kd \tag{2.10}$$

$$\hat{\alpha} = \alpha d \tag{2.11}$$

$$\hat{\omega} = \omega\sqrt{m/\kappa} \tag{2.12}$$

$$\hat{\gamma} = \gamma/\sqrt{\kappa m}, \tag{2.13}$$

yields dimensionless equations governing dispersion relations,

$$\hat{\omega} = \hat{k}^2 - \hat{\alpha}^2 + 2\hat{k}\hat{\alpha}\hat{\omega}\hat{\gamma} \tag{2.14}$$

$$0 = 2\hat{k}\hat{\alpha} + (\hat{\alpha}^2 - \hat{k}^2)\hat{\omega}\hat{\gamma}. \tag{2.15}$$

Solving equation. (2.14) and (2.15) for $\hat{\alpha}$ and $\hat{k}$ in terms of $\hat{\omega}$ and $\hat{\gamma}$ yields

$$\hat{\alpha} = \hat{\omega}^2 \frac{\hat{\gamma}}{\sqrt{2}} \left\{ \left[1 + (\hat{\omega}\hat{\gamma})^2\right] \left[1 + \sqrt{1 + (\hat{\omega}\hat{\gamma})^2}\right] \right\}^{-1/2} \tag{2.16}$$

$$\hat{k} = \hat{\omega} \frac{1}{\sqrt{2}} \frac{\left\{ \left[1 + (\hat{\omega}\hat{\gamma})^2\right] \left[1 + \sqrt{1 + (\hat{\omega}\hat{\gamma})^2}\right] \right\}^{1/2}}{1 + (\hat{\omega}\hat{\gamma})^2} \tag{2.17}$$

These solutions depends on the dimensionless product of $\hat{\omega}\hat{\gamma}$. For $\hat{\omega}\hat{\gamma} < 1$, equation (2.16) and (2.17) predict $\hat{\alpha}/\hat{\omega} \propto \hat{\gamma}\hat{\omega}$ (i.e., $\alpha \propto f^2$) and $\hat{c} \equiv \hat{\omega}/\hat{k} =$ constant. For $\hat{\omega}\hat{\gamma} > 1$, they predict $\hat{\alpha}/\hat{\omega} \propto (\hat{\gamma}\hat{\omega})^{-1/2}$ (i.e., $\alpha \propto f^{1/2}$) and $\hat{c} \equiv \hat{\omega}/\hat{k} \propto (\hat{\gamma}\hat{\omega})^{1/2}$. These capture the regimes shown in Figure 1.1, particularly for the absorption coefficient α. The crossover frequency of $f^* = \omega^*/2\pi \approx 10^4$ Hz, which is determined by the condition $\hat{\gamma}\hat{\omega} = 1$.

Note that the scaling behavior of α for the 1D model agrees with the experimental data shown in Figure 1.1. The scaling behavior for c shows a flat region and then an increase with power law exponent 1/2. This agrees with Figure 1.1 for low frequencies but not high frequencies, where only a moderate increase is observed.

2.2.2 Physical Values of Parameters

Since it will be useful to estimate κ and γ of real systems, here we demonstrate how κ can be connected to the granular properties. Using hertzian contact mechanics, the force between two particles of the same elastic modulus E but possibly differing radius $R = d/2$ is not a linear spring but instead a nonlinear spring, with force law

$$F = \frac{4}{3} E^* {R_{\text{eff}}}^{1/2} \delta^{3/2}$$

where

$$\frac{1}{E*} = \frac{1 - \nu_1^2}{E_1} + \frac{1 - \nu_2^2}{E_2}$$

and E_1, E_2 are the elastic modulus and ν_1, ν_2 are the respective Poisson's ratio of each particle Since both particle have same E, $E^* = E/2(1 - \nu^2) \approx E/2$ if $\nu \sim 0.25$ or smaller and $R_{\text{eff}} = 1/(1/R_1 + 1/R_2) \approx R/2$ if $R_1 \approx R_2 \approx R$. Thus,

$$\kappa \equiv \left.\frac{dF}{d\delta}\right|_{\delta_0} = E\sqrt{\frac{R\delta_0}{2}}$$

The value of δ_0 is set by the confining pressure, $P_0 = F_0/d^2 = F_0/4R^2$. This yields:

$$4R^2 P_0 = \frac{2}{3}E\sqrt{\frac{R}{2}}{\delta_0}^{3/2}.$$

Solving this equation for δ_0 gives

$$\delta_0 = \left(6\sqrt{2}\sqrt{P_0/E}\right)^{2/3}$$

and

$$\kappa \approx 0.72Ed\left(\frac{P_0}{E}\right)^{1/3}. \tag{2.18}$$

For sediments, $E \approx 50$ GPa (5×10^{10}), $d \approx 0.1$ mm (10^{-4}), $P_0 \approx (\rho_s - \rho_l)gh$, where $g \approx 9.8$ is the gravitational acceleration and h is the depth of the sediment in question. If we assume $\Delta\rho \approx 1000$ and $h \approx 10$ cm, then $P_0 \approx 100$ Pa. Plugging these values in gives:

$$\kappa \approx 5\times10^{10}\times10^{-4}\left(\frac{10^2}{5\times10^{10}}\right)^{1/3} \approx 6\times10^3 \text{ N/m}$$

We note that even increasing the depth by an order of magnitude, raising P_0 by an order of magnitude, only increases κ by a factor of 2. Thus, value of κ is only weakly dependent on h via $h^{1/3}$. Additionally, note that $\kappa \approx 6\times10^3$ N/m is considerably smaller than what would be estimated from simple dimensional analysis, $\kappa \approx Ed \approx 5\times10^6$ N/m. This follows directly from Hertzian contact mechanics.

CHAPTER 3:
Methodology

This chapter will layout our 3D simulation methodology and considerations behind each steps. It will cover 1) setting up the channel with spherical atoms/particles to our desired sizing, 2) packing of the atoms using a confining pressure to diminish existing kinetic energies present within the system, 3) introducing longitudinal and transverse waves into the channel via the lower boundary wall and 4) analyzing the results and effects using MATLAB, illustrated by the picture below.

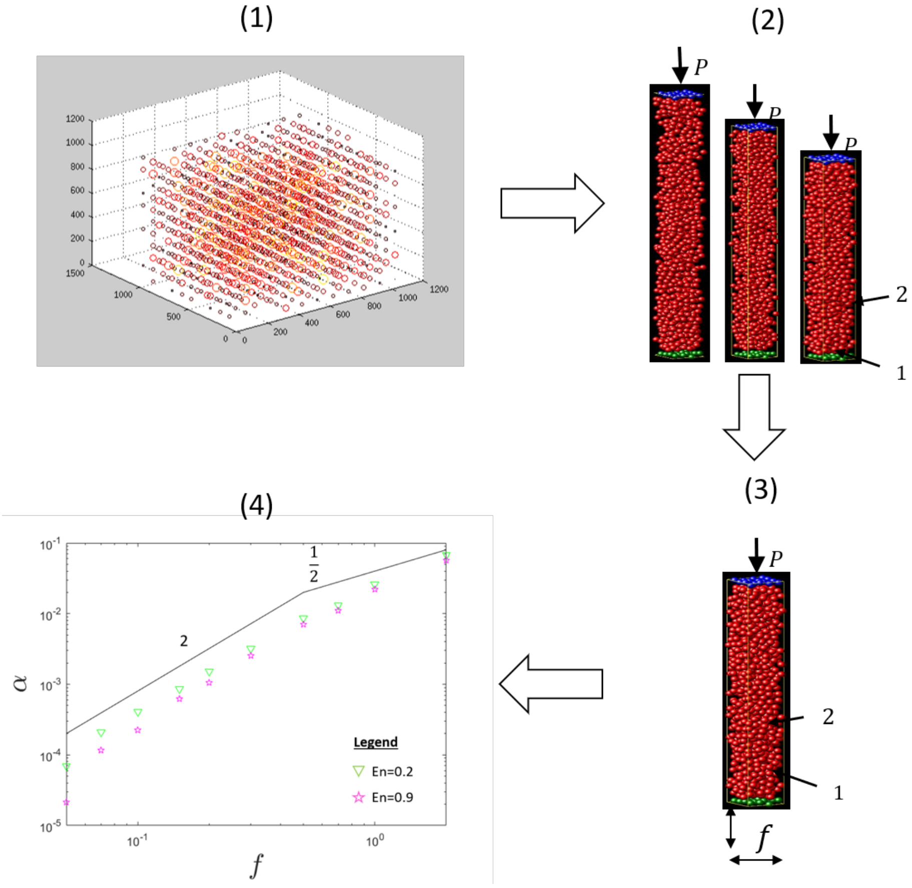

Figure 3.1. Simulation flowchart

3.1 Discrete Element Modelling

DEM is a numerical method used in modelling motion of distinct particles within a system. There are numerous DEM software in the market. In our paper, we used an open source DEM package called LAMMPS (Large-scale Atomic/Molecular Massively Parallel Simulator). The simulator was chosen due to its usefulness for particle based modeling of materials at length scales ranging from atomic to mesoscale and to continuum [22]. On top of that, it had the capacity to conduct large scale simulations which were particularly important in sediment acoustics and also the ability to run on any platform ranging from a single CPU core to supercomputers.

More importantly, LAMMPS has built in force-law packages that enable us to capture vanishing small inter-particle overlap that were of utmost importance for our theory. Integrated with springs and dashpot like simulators in the codes, it generated a kinematics of the particles that were updated within an explicit time integration scheme, based on the net forces on a single particle taking into account the inter-particle forces with its neighboring particles.

3.1.1 Setting up Granular Model in LAMMPS

A granular model in LAMMPS is composed of spherical atoms with a diameter,d. This will allow us to account for angular velocity and torque which in turn caused the atoms to rotate. We ran our simulation using ‘atom_style sphere’ whereby we could define the attributes of the sphere using diameter, mass and angular velocity. We then established our simulation using Hookean model based on law of elasticity where the size of deformation is directly proportional to the deforming force as described in (3.1). In our simulation model, we will ignore the tangential forces with κ_n and γ_n equate to κ and γ respectively in our equation 2.4.

The Hookean styles package built in LAMMPS was described as [22] :

$$F_{hk} = (\kappa_n \delta \mathrm{n_{ij}} - m_{\mathrm{eff}} \gamma_n \mathrm{v_n}) - (\kappa_t \Delta s_t + m_{\mathrm{eff}} \gamma_t \mathrm{v_t}) \tag{3.1}$$

whereby subscript n represent the normal component and t represent the tangential component. κ is the elastic constant, δ is the overlap distance, γ is visco-elastic damping constant,

v is the relative velocity, $\mathrm{n_{ij}}$ is the unit vector along the line connecting the centers of two particles,subscript ij, and Δs_t as the tangential displacement vector. The first parenthesized term in equation (3.1) represent the normal force that has both the contact force and damping force within. The second parenthesized term therefore represents the tangential force with shear and damping force components. Simulation parameters κ has units of (force/distance) and γ has units of (1/time).

3.2 Modelling Methodology

This section covers the details of the simulation flowchart illustrated in Figure 3.1. We used three different programs in the entire simulation workflow, namely MATLAB, LAMMPS and Python. MATLAB was generally used to create the channel with desired particles fit parameters as well as creating plots from the data output from LAMMPS. LAMMPS was the key program that resolve the inter-particle interactions of our simulations and created large data output for our analysis. A python script was created and clean up the large data output to make it readable by MATLAB for post processing. Apart from programming software, we also leveraged on NPS's HPC supercomputers to run large scale simulations within a relatively short period of time that optimized the entire simulation process. Despite the impracticality of small system size in real time environment, we experimented our simulation process using a very small system size (i.e., N=1000) to ensure it was workable before experimenting it on larger system sizes (i.e., N=50000).

3.2.1 Creating the Channel

The first step in the modelling was to create a predefined system size of atoms/particles (hereby termed as probe atoms) with similar radii. A MATLAB code appended in Appendix A was developed to set the system size and its boundaries The boundary of the system was created with similar spheres atoms but with larger radii to (1) differentiate the boundary and probe atoms, (2) prevent slipping through of probe atoms during the simulations. A total of three different atom types were used in our experiment where Type 1 was the probe atoms and Type 2 (lower wall) and Type 3 (upper wall) were the boundary/wall atoms. Input parameters such as number of atoms and width of square channel are abbreviated as N and W respectively and a sample of the output can be seen in Figure 3.2. Additionally, a output file with the positions of each atom was generated.

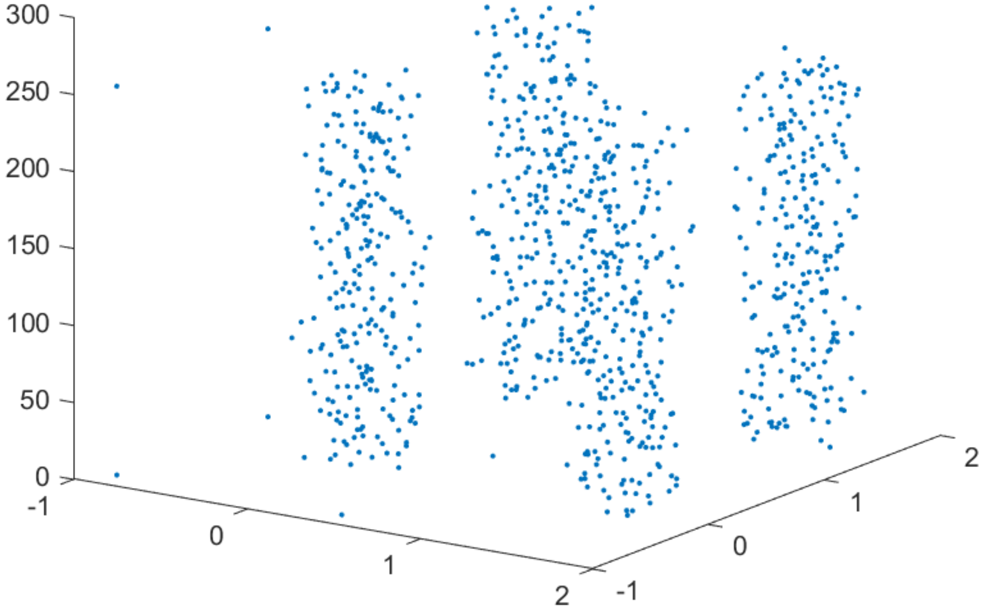

Figure 3.2. Illustration of output from MATLAB for system size of N=1000 with W=3

3.2.2 Compressing the Channel

To achieve persistent contacts between particles as described in hertzian contact theory, we compressed the channel via a confining pressure until kinetic energy within the system diminishes. We first begin by inputting the positions coordinates generated from MATLAB into LAMMPS where LAMMPS will created the exact same channel with its corresponding atom's positions. A constant force was applied on the top boundary wall that gradually lower the top wall and compacting the probe atoms into an organized network of atoms as illustrated in Figure 3.3. The compression force on the upper boundary wall were built in within the LAMMPS code in Appendix B and remained constant through the various simulations.

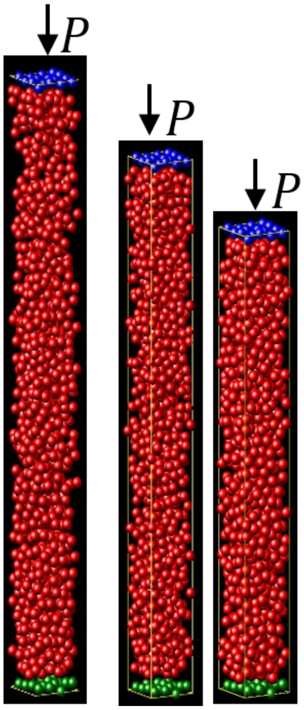

Figure 3.3. Schematics for compression of long channel

A loop was created within the codes to continue the compression till no significant kinetic energy were present within the system. The simulation continues until a steady state is achieved. A output file generated at the end of this simulation provides us with the updated three dimensional position coordinates of each particle, whereby persistent contacts are present. The linear spring dashpot in the simulation was controlled by input parameters shown in Table 3.1. The input parameters E and P will always diff by a factor of 100 to ensure that the parameters used in our simulations are realistic in application. This set the value of κ, linear spring constant, in the simulation.

Table 3.1. List of input parameters for generating initial conditions

Input Parameters	Abbrev.	Values(Non-Dimensional)
Number of Atoms	N	1000, 5000, 10000, 50000
Width of Channel	W	3, 5, 7
Young Modulus	E	1000
Pressure	P	10

3.2.3 Generating Transverse and Longitudinal Waves into Channel

A separate LAMMPs code in Appendix C will then reestablish the positions of each atom in the simulation by reading the dump file generated. Longitudinal waves were created by oscillating the lower boundary wall in the z- direction whilst transverse waves were achieved by oscillating in the x-direction as shown in Figure 3.4. The magnitude and frequency of oscillation were controlled by simulation parameter A and f respectively. In both instances, the upper boundary wall was fixed by a confining pressure. The oscillatory motion in both x and z direction will simulate a wave-like signal travelling through the channel akin acoustics waves hitting the seabed bottom. Probe atoms within the channel will be pre-identified in the codes such that we were able to study the attenuation losses as the waves travelled through the channel. A total of 90 probe atoms was used for a system size of $N = 50000$. We identified 60 probe positions from the first 30000 atoms and remaining 30 probe positions from the last 20000 as we expected to see more variances in the results at the beginning of the channel since wave energy diminishes as it travel through channel.

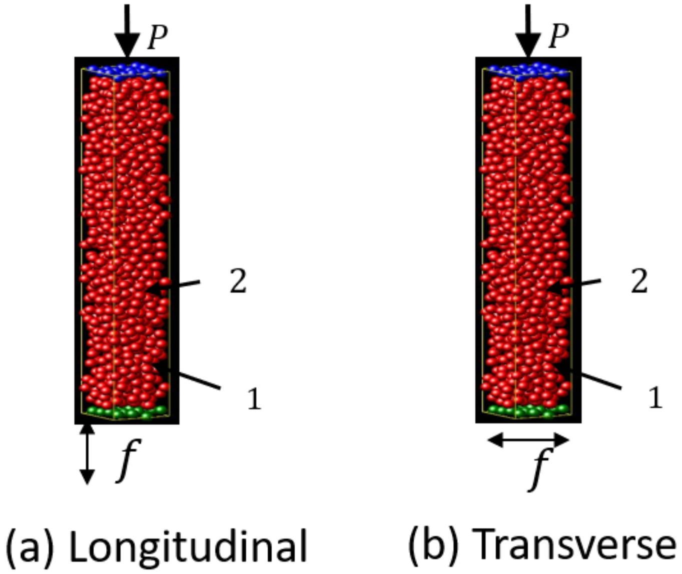

Figure 3.4. Schematics of generating (a) longitudinal and (b) transverse Waves within the channel.

The amplitude of the simulation was set constant at a small magnitude relative to its overlap to better observe its variability. E and P remained consistent with previous simulation and N and W were varied accordingly for comparison purposes. Particularly, in order to validate the practicality of our simulation model in real-time environment where seabed bottom are typically considered as an infinite system, we will have to define the large system limits. To do these, we chose to fix our system size at $N = 50000$ and ran the simulations with different channel width which directly corresponding to its channel length. In essence, a large channel width will generate a shorter channel. The list of input parameters used in running this simulation are shown in Table 3.2 will allow us to study the various effects on wave attenuation across the channel. The oscillations of the boundary wall were achieved by adjusting the boundary wall settings in Appendix C.

By introducing longitudinal waves into the channel, we examined the effects of compression losses or normal forces. In this instance, we were particularly interested in the z-displacement of each probe atom. For transverse waves, we extracted both x and z displacement to analyze the effects of shear within the channel. The list of values for f will allow us to establish the frequency dependency effects of the signal. The dashpot constant,γ, was adjusted using simulation parameter, restitution coefficient e_n, to analyze its effect on dispersion based on our theory.

Table 3.2. List of input parameters for generating impulse

Input Parameters	Abbrev.	Values(Non-Dimensional)
Amplitude	A	0.0001
Frequency	f	0.05, 0.07, 0.1, 0.15, 0.2, 0.3, 0.5, 0.7, 1, 2
Restitution Coefficient	e_n	0.1,0.2,0.5,0.8,0.9
Number of Atoms	N	1000, 5000, 10000, 50000
Channel Width	W	3, 5, 7
Young Modulus	E	1000
Pressure	P	10

3.3 Data Processing

The above sets of simulations generated an enormous set of raw data (position coordinates and force components) that requires data processing to extract required data for analysis. A python script in Appendix 4 was used to extract only the position coordinates with its respective probe atom ID to facilitate data processing in MATLAB.

The final step was to create plots using those data to study the dispersion relations, similar to those shown in Figure 1.1. To study the effects of normal forces, we used MATLAB to plot the maximum z-displacement of each identified probe atoms as a function of time by extracting the first peak of the wave signal where we expect to see a gradual decay over time. To demonstrate the frequency dependence relationship, we created a plot to compare the rate of attenuation by different frequencies. To correlate with the experiment data set used to validate our hypothesis, we also generate a plot to study the wave speed as a function of frequency. This was repeated for transverse waves but we studied the effects both in x and z direction. In order to study the define the large system limits, we ran the longitudinal and transverse waves simulations on different channel width to establish its in-dependency such that they are realistic in applications. Lastly, we ran the simulation with different magnitude of the dashpot term, γ, by adjusting the simulation parameter e_n. The results and analysis will be discussed in the next chapter.

THIS PAGE INTENTIONALLY LEFT BLANK

CHAPTER 4:
Results and Discussion

In this section, we will discuss the results of the numerical simulations detailed in the previous chapter. Waves appear in two forms, transverse and longitudinal. Hence, we will present the effects of compression waves (longitudinal) followed by shear waves (transverse) in the channel. We will then define the large system limits that are useful to justify the reliability of our simulation model in real time environment where marine sediments are considered as an infinite system. Lastly, we will explore the effects of γ, physically bounded by parameter e_n, that in our theory will control the magnitude of the dashpot used to simulate the dissipative forces due to compression losses.

4.1 Effect of Compression Waves

We will first study the effect of longitudinal waves that are critical in examining our hypothesis that compression losses, due to grain-grain interactions, are a key loss mechanism in signal attenuation in marine sediments. To validate our theory and simulation model, our results should produce the same dispersion relations from experimental data shown in Figure 1.1.

4.1.1 Frequency Dependence Attenuation and Sound Speed Ratio

By generating a plane wave signal in the z direction across the channel by vibrating the lower boundary wall at a particular frequency, we will expect the amplitude of the signal to decrease gradually as it transverses through the channel in a finite system. In our simulation with largest system size of $N = 50000$, the wave signal will not diminish fully at the end of the channel, hence we observed a subsequent spike in wave signal after the initial peak resulted from waves bouncing off the upper wall at the end of the channel. In our simulation, we captured the first peak of the signal and observed that the amplitude of the signal decreased as the waves transverse through the channel as per our hypothesis (See Figure 4.1). The plot shown the peaks of the three selected probes particles $[i = 1, 5, 10]$ with good separation to clearly the attenuation effects. These trends were similarly observed as we varied the our simulation over the set of 10 different frequencies.

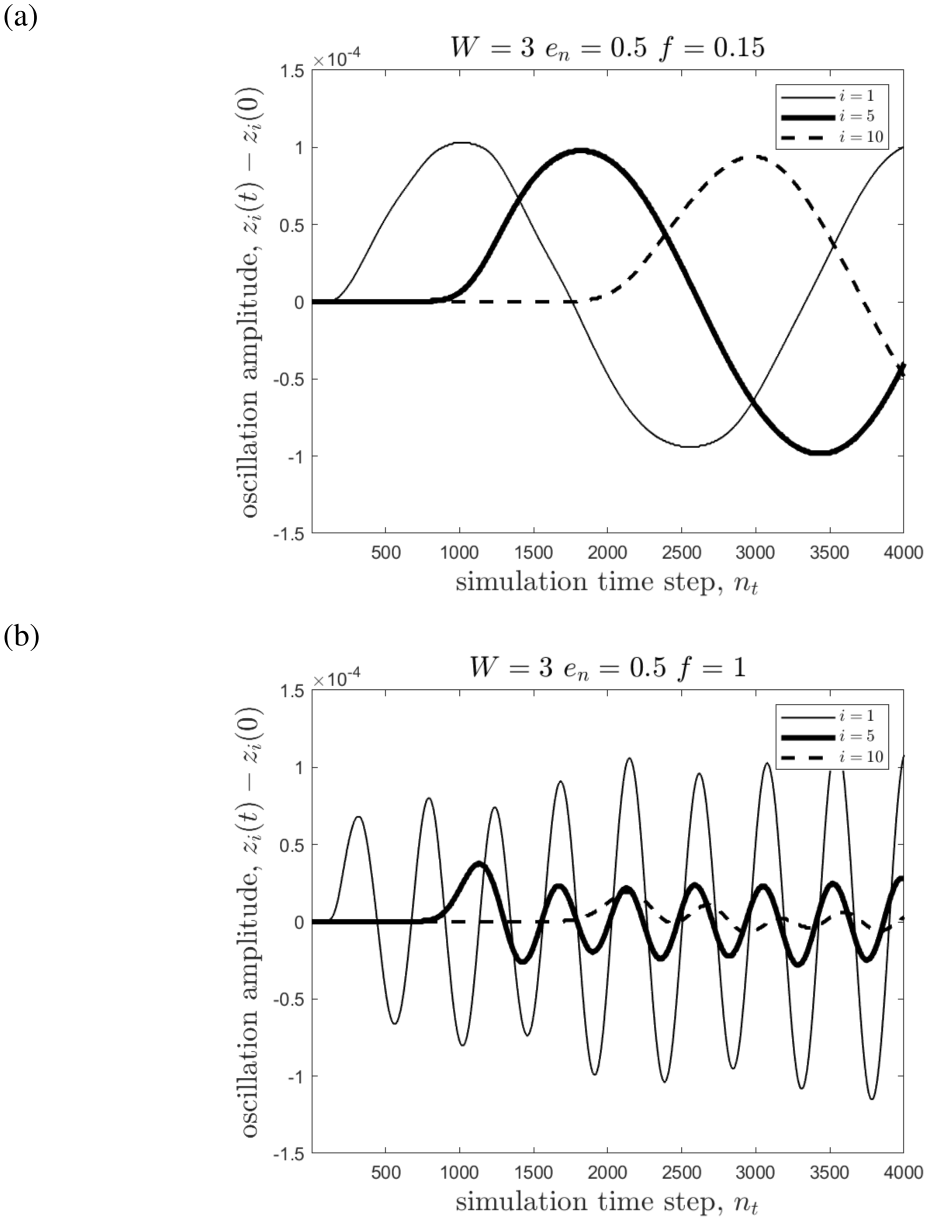

Figure 4.1. Comparison of attenuation rate in oscillation amplitude with (a) low frequency and (b) high frequency

In Figure 4.2, we plotted the max displacement of all probe particles in log scale as a function of z with three non-dimensional different frequency (0.05,0.2 and 1) to resolve the rate of attenuation for different frequency, represented by attenuation coefficient $\alpha(f)$. The rate of signal attenuation increases with increasing frequency therefore established the frequency dependency relation on signal attenuation.

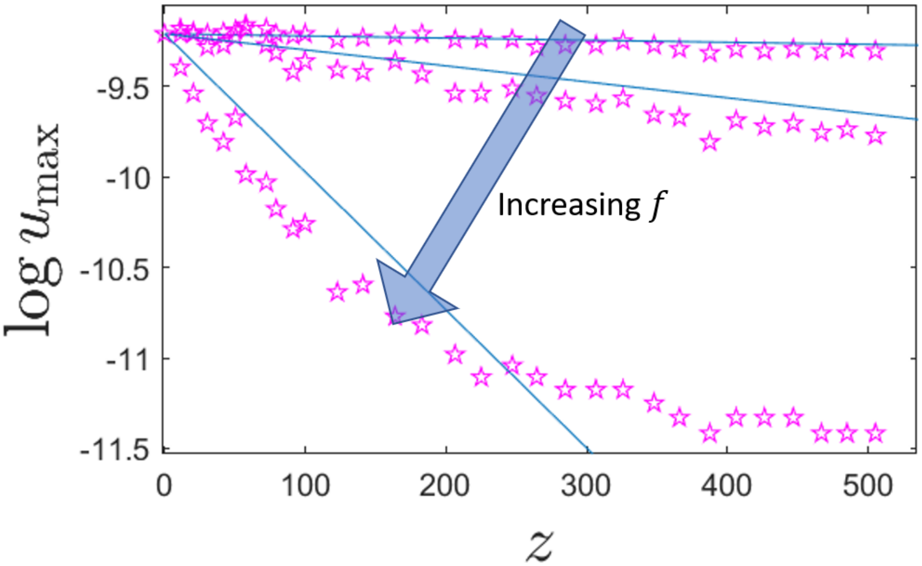

Figure 4.2. Maximum displacement observed along the channel for $e_n = 0.9$

In order to show the relationship, we leveraged on dimensional analysis to plot the non-dimensional units in order to show the frequency dependence relationship of attenuation coefficient and sound speed ratio. In Figure 4.3, our simulation results generates similar scaling behavior as the experimental data used in our paper. At low frequencies, the attenuation coefficient follows f^2 power law relationship, and bends over to $f^{\frac{1}{2}}$ at the higher frequencies simulation parameters. The compressional waves created from the oscillation of the boundary wall created kinetic energy within the system. The compression effects were measured from the magnitude of the displacement and in our theory, the magnitude of this displacement affects the force components resulting from the inter-particle interactions. As force chains propagates through the channel, the magnitude decreases over time and distance as shown from the previous plots. The higher the frequency, the larger the magnitude of the forces in a single particle within the systems. This can be observed from the linearly increasing rate of loss, otherwise termed as attenuation, from a relatively small frequencies. This energy loss accounts for the dissipated compression forces that validated our hypothesis that repulsive forces from grain to grain contacts has an substantial effects on the attenuation of signal in marine sediments. Even by considering this effect alone, we were able achieve the same scaling behavior. We note that this constitutes the main result of this thesis. Specifically, a simple, grain-grain compression loss term is able to reproduce the functional form of the experimentally observed dispersion relations in 3D grain-based simulations.

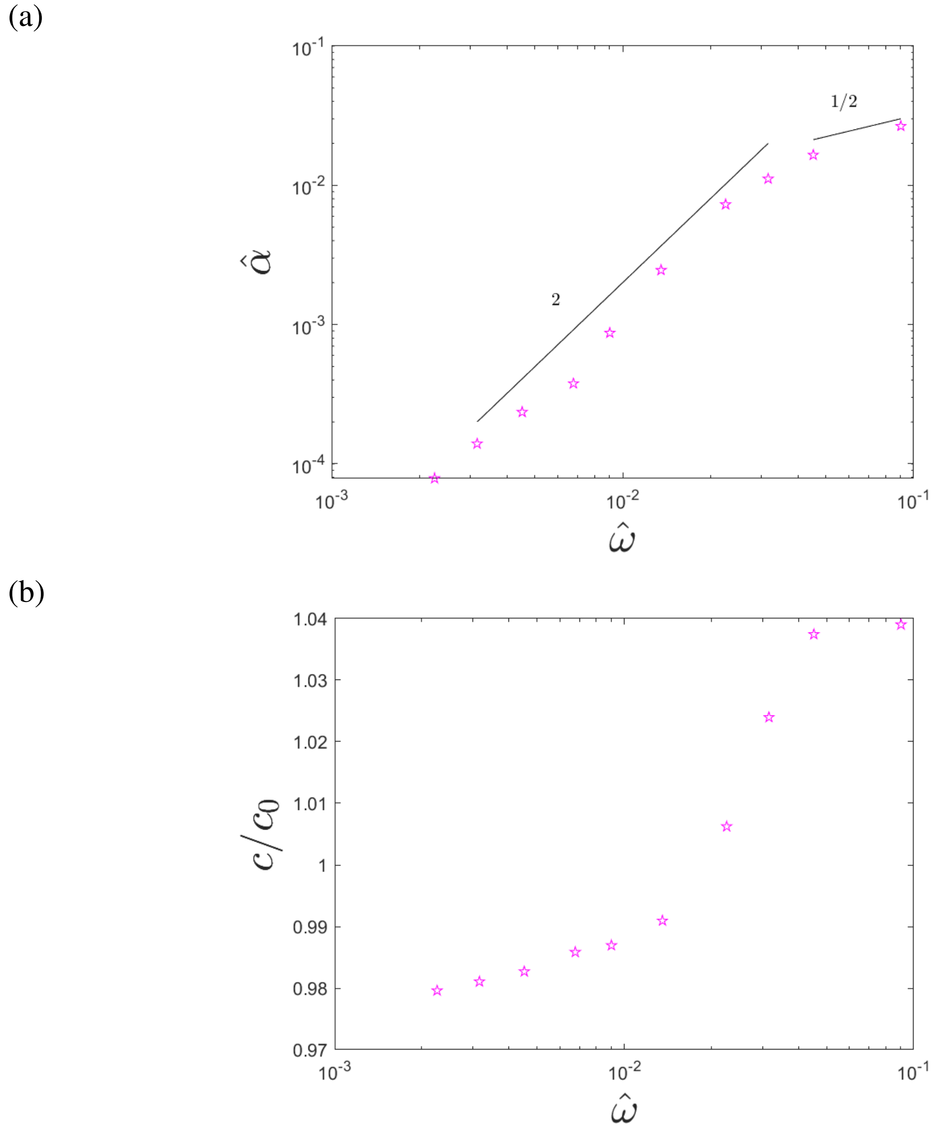

Figure 4.3. Scaling behavior for (a) $\hat{\alpha}(f)$ and (b) $\hat{c}$ for $e_n = 0.9$

Sound speed dispersion in marine sediments has major impact on the applications of sonar systems. Direct measurement from field were often conducted using wave-guide at high frequency band (ranging from 10kHz to 1MHz). Measurement at low frequency band is not commonly conducted since experimentally challenging to detect the variability at low frequency (below 1kHz) [23]. In order to measure the variability at low frequency in physical experiments, the distance between embedded probes are comparatively small to the wavelength, and its signal energy loss over the short propagation path is too small to be accurately measured [23]. In our simulations, we experimented with both low and high frequencies in order to achieve the same scaling behavior from experimental data. Figure 4.3 plotted using dimensionless quantities illustrated a sound speed dispersion curve with restitution coefficient of $e_n = 0.9$ that constrained the value of γ in our theory. γ value in our simulation correspond to 2.14. The restitution coefficient of dry sand ranges from 0.88 to 0.98. At low frequency band with dimensionless parameter f of the following values [0.05 0.07 0.1 0.15 0.2 0.3], sound speed ratio remains constant with only 0.01 variability. A distinct spike was then observed at higher frequency band with non-dimensional $f = 0.5, 0.7, 1, 2$. $\hat{\omega}$ is directly related to the value of non-dimensional f with $\hat{\omega} = 2\pi f$. As a whole, the frequency dependence sound speed ratio, $\hat{c}(\hat{\omega})$ scaling behavior was similar to the experimental data used.

4.2 Defining Large System Limits

With DEM simulations, we used a discrete approach that is based on the analysis of motion of each particles within the finite system that removed the need for global assumptions such as steady state behavior or uniform constituency [24]. In this instance, we are using a finite discrete particles to represent a quasi-infinite environment using periodic boundary conditions in the transverse direction, i.e., seabed bottom. To resolve infinite problem practically, it is important that we defined the large system limits of our simulations to prove that the results and quantities are independent of the system size/channel length. Simulations were set to $N = 50000$ for time practicality consideration as the larger the system size, the longer computational time it is required per simulation. Henceforth, to evaluate the large system limits, we kept the system size consistent and adjusted the channel width then will directly influence the length of the channel. The larger the channel width, the shorter the channel will be in the z direction. By doing so, we were able to determine the suitable channel length to mirror infinite system in simulations. For example, if a shorter channel length (with $W = 5$) simulation results were the same as that of a longer channel length (with $W = 3$), we can henceforth use the shorter channel length as the large systems limits in our simulation. The independence of the system size/ channel width increased the reliability of our theory and the practicality of our simulation model.

In Figure 4.4, we randomly selected three probe particles $[i = 1, 5, 10]$ from our simulation and studied their attenuation as the transverse waves travelled through the channel. The large the i value, the further is the probe particle from the lower boundary wall. By varying the channel width, the position of each i corresponds to different position in the z direction. With a smaller channel width, the position of the probe particle were further down the channel as compared to a larger channel width. Figure 4.4 (a) shows a significant drop in oscillation amplitude as compared to the other two plots due to energy losses as the waves travel through the channel in the z direction. On the contrary, a large channel width will have the same probe particle nearer to the vibrating wall, hence exhibiting oscillation amplitude close to the excitation amplitude used in our simulation, $A = 10^{-4}$.

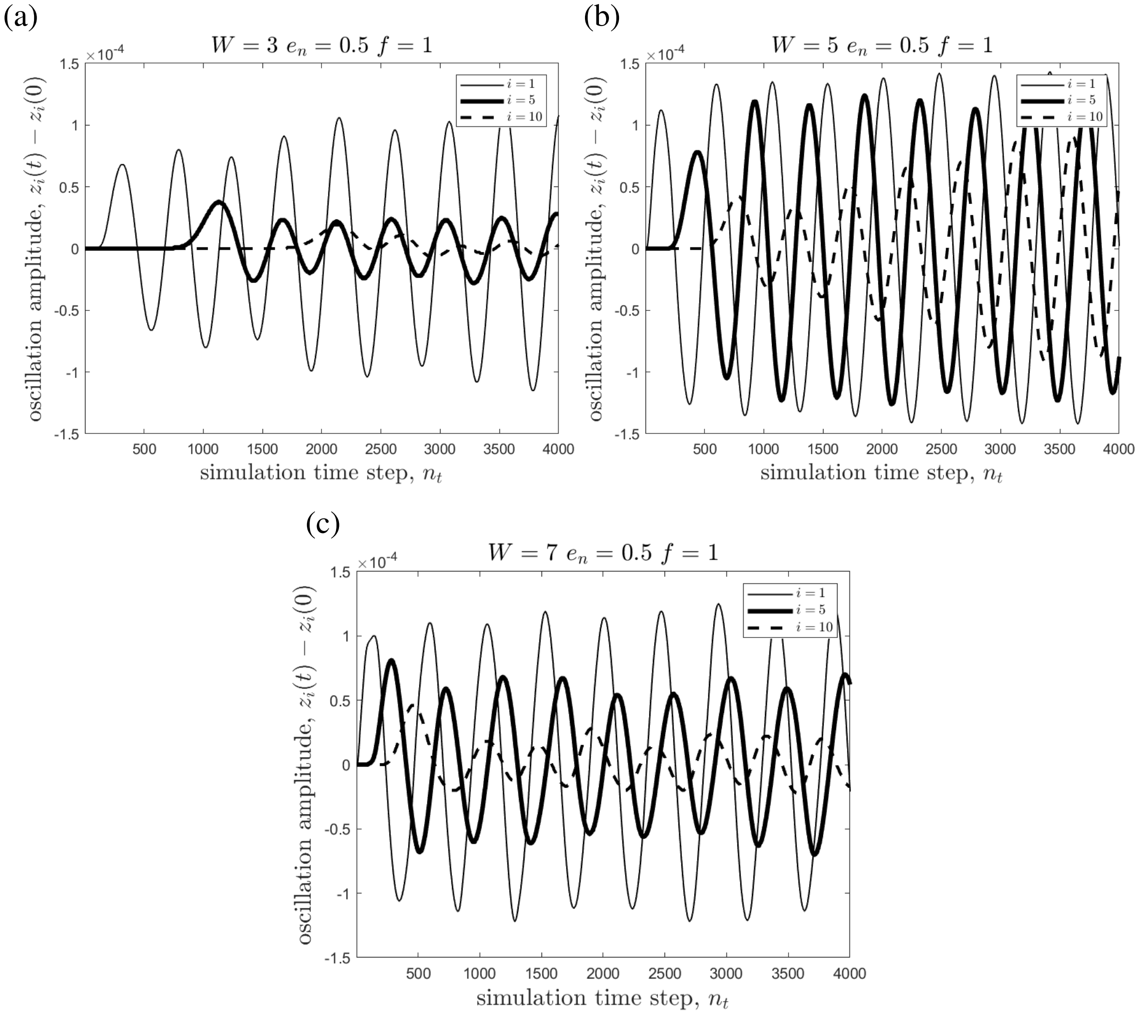

Figure 4.4. Oscillation amplitude of (a) $W = 3$, (b) $W = 5$ and (C) $W = 7$ with $f = 1$ and $e_n = 0.5$

As seen in Figure 4.5, the frequency dependence attenuation continues to follow the same power law relationship across the three different channel width. These results give confidence that the simulation methodology are practical in simulating the real time environment of seabed bottom where they are infinite system size. In defining the large system limits, the results from $W = 3$ and $W = 5$ appeared to be more stable and consistent as compared to W7 which has the shortest channel length. In general, the sound speed dispersion plots were aligned with experimental data since they were generally constant at low frequency and peaked at higher frequency. For $W = 7$, there were several points that behaved irregularly and were removed from the plots shown. As these plots were generated using a polynomial fit, coupled with extremely small variations between each probe particles, it is inherently challenging to plot each point with precision. With that, we can also conclude that simulations should at least be done with channel width of 3 or 5. It appeared that $W = 7$ does not fit the large system limits in our simulation due to the short channel length. Henceforth, majority of the simulations and results discussed henceforth were done using $W = 3$ for consistency in comparison. Longer system sizes could be examined in the future with a larger computer cluster.

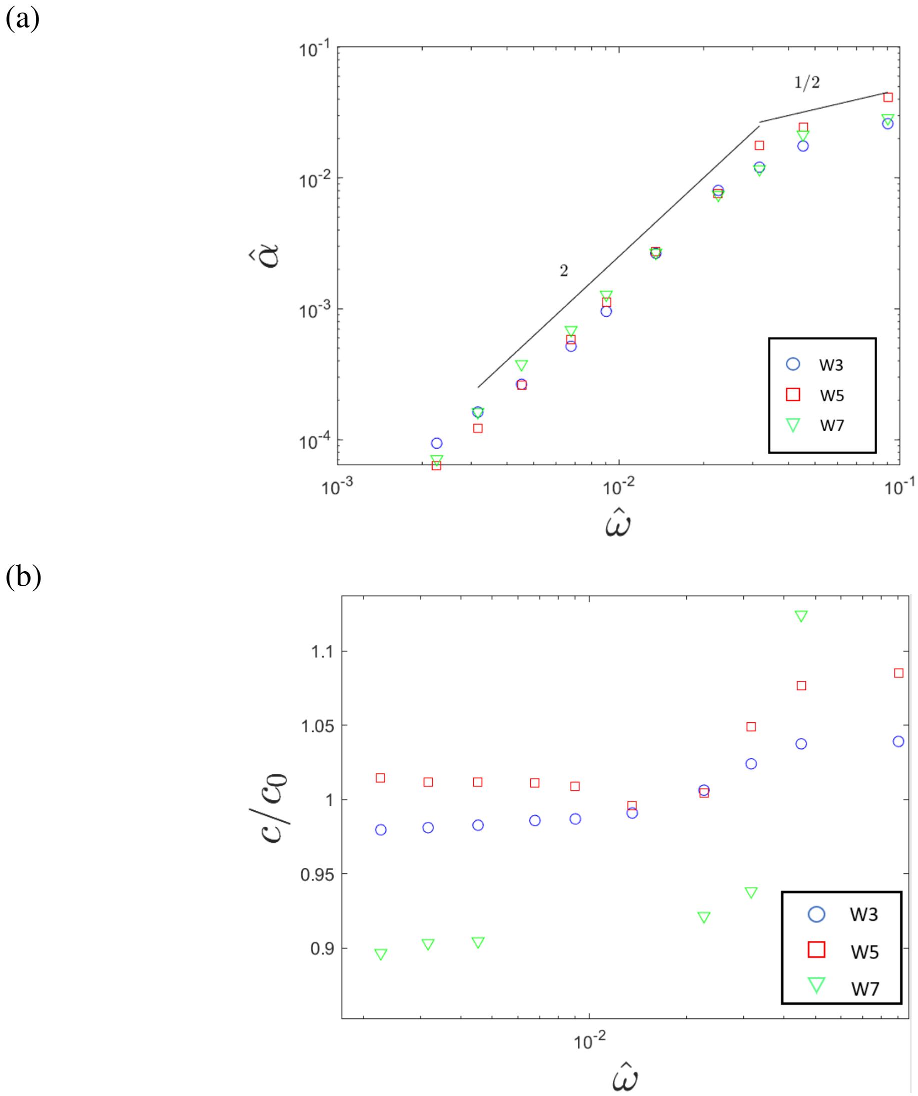

Figure 4.5. Comparison of different channel length and its effect on attenuation (Top) and sound speed dispersion (Bottom) for $e_n = 0.5$.

4.3 Effects of Shear Waves

In the section above, we studied the effects on the particles when compressional waves are introduced in the channel. We will now study the other type of waves, shear (or transverse) waves and its corresponding effects on the channel. This section will study the effects of transverse waves achieved by moving the lower boundary wall in the transverse direction

(x) in our simulation model. The effects on the particle are controlled by the shear modulus which is the ratio of shear stress and shear strain. In sediment acoustics application, shear waves are often associated with frictional losses between grains. Preliminary results showed that the presence of shear effects despite the complete lack of tangential forces in our simulation model as described in section 3.1.1. Even frictionless packing of grains have shear rigidity that can support propagating shear waves.

4.3.1 Frequency Dependence Attenuation and Sound Speed Ratio

We repeated the same processes by observing the attenuation in oscillation amplitude of the waves travelling through the channel. In this section, we analyzed both the displacement of particle in x and z direction resulted from shearing the boundary wall in the transverse direction with a low ($f = 0.15$) and high ($f = 1$) dimensionless frequency to analyze the signal attenuation effects. Similar frequency dependence effects were observed in transverse direction with higher attenuation at high frequency and vice versa. These effects are similar to shear waves effects when propagating through the channel. However, we observed a non-linear oscillation in the z direction as the second probe particle ($i = 5$) has a higher amplitude than the first probe particle and the plots no longer follows a smooth sine curves which was very apparent at the lower frequency. Figure 4.6 and 4.7 shows the signal behavior at low and high frequency, respectively. Measurements in the alternate direction of waves direction, i.e., longitudinal direction are not common in this field of research but the results were interesting to note and discuss. The grain to grain interactions caused coupling of x and z force components.

(a)

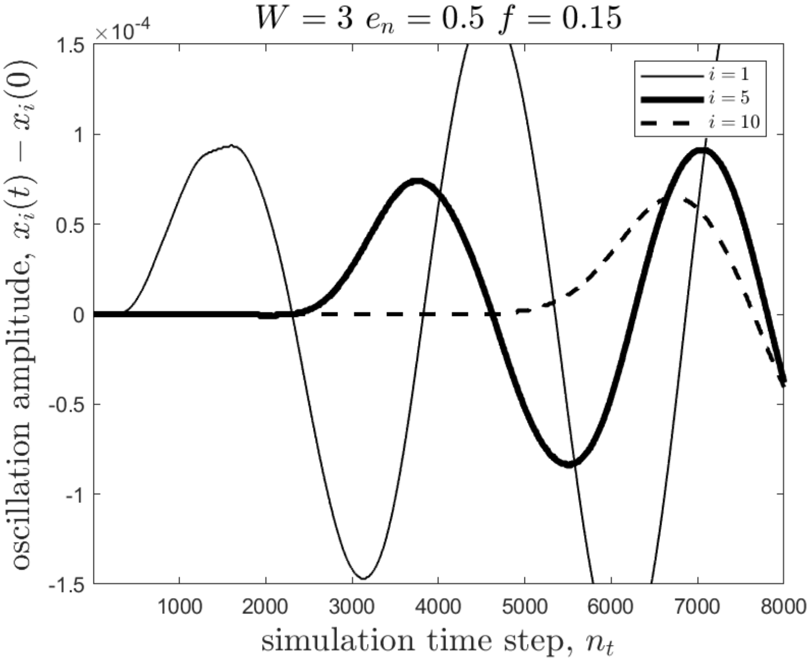

(b)

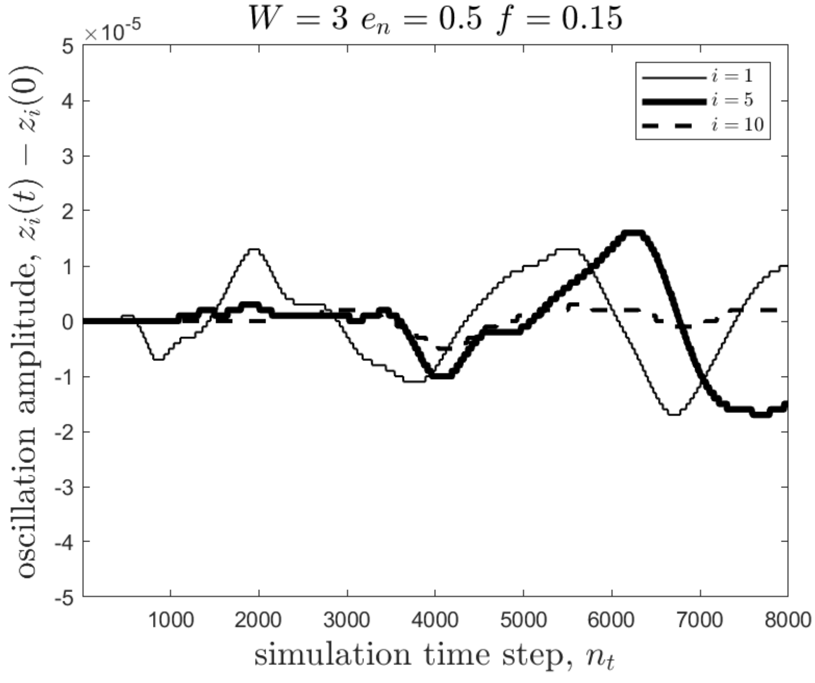

Figure 4.6. Shear effects in x and z direction at low frequency, $f = 0.15$

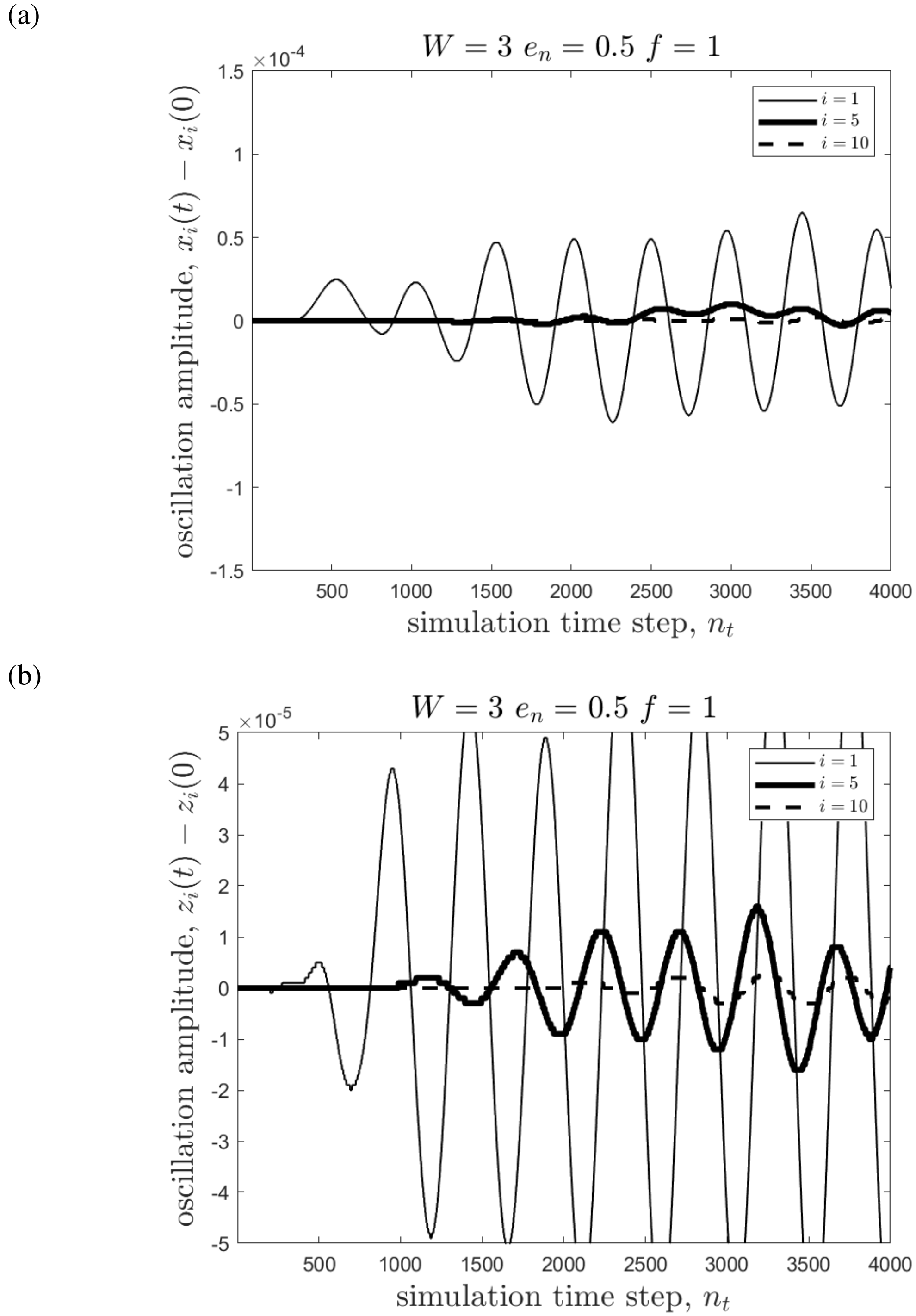

Figure 4.7. Shear effects in x and z direction at high frequency, $f = 1$

In 3D simulation, the effect of shearing of the boundary wall will have components of motion on each particle in all three directions as illustrated in the pictorial in Figure 4.9. Each inter-particle interaction are different and dependent on the granular packing henceforth resulted in the non-linearity displacement in the z direction due to shear waves propagating across the channel. This effects highlighted the need to consider the type of granular packing methods used and its associated effects on forces in our simulations. By extracting the z-displacement on each system particle, we were able to analyze the compression effects on a particle generated from a harmonic oscillating shearing motion by the lower boundary wall. We also observed that the behavior of displacement in z is non-linear in both channel width of 3 and 5 that re-affirmed our previous analysis on large system limits.

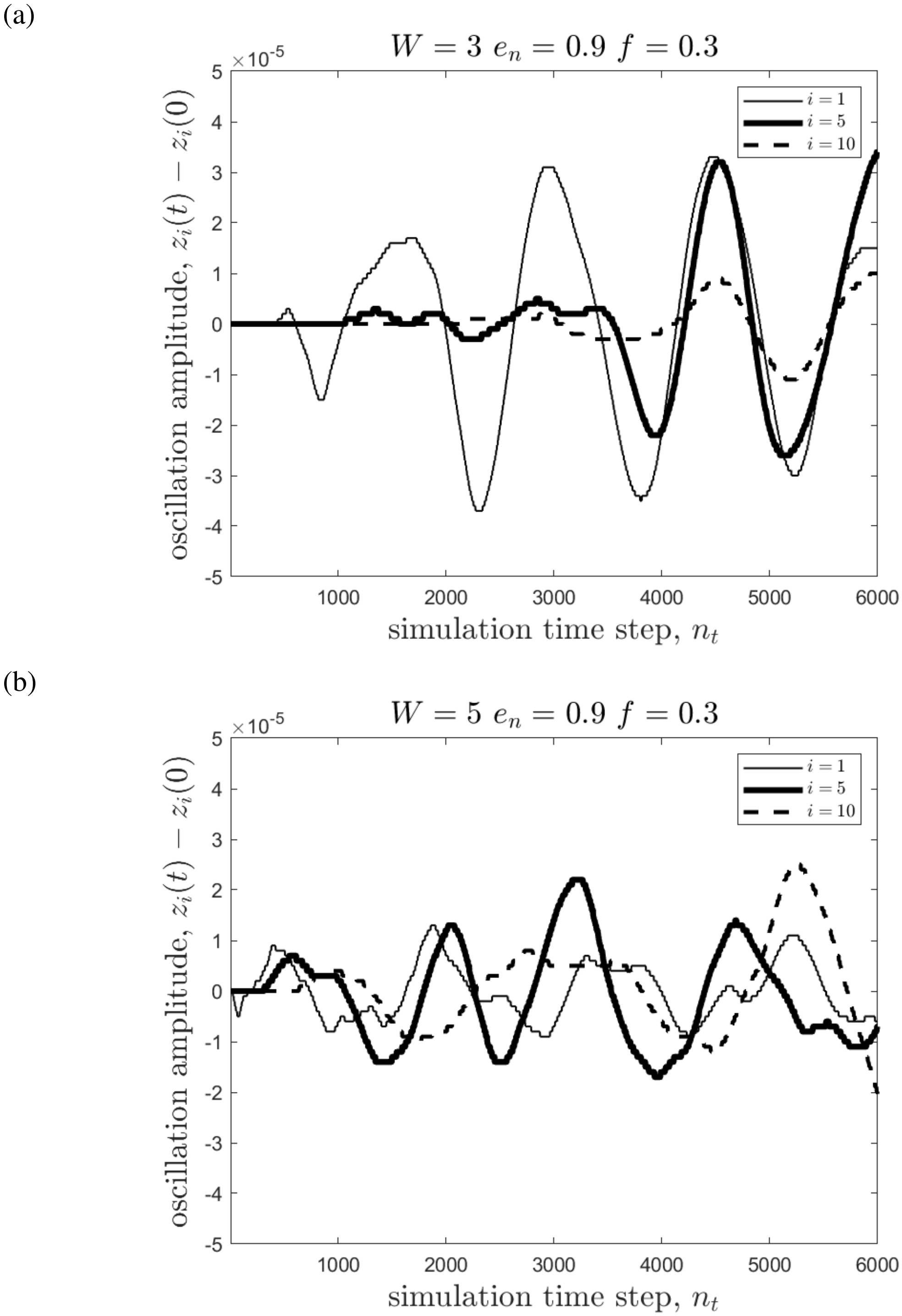

Figure 4.8. Shear effects in z direction in different channel length

The attenuation coefficient and sound speed ratio with respective to its frequency are plotted in Figure 4.10. While the scaling behavior do not correlate as well with scaling behavior of experimental data, the general trend of plots did seem to suggest that both shear waves and compression waves behaved rather similarly. Despite that, there were some notable effects of shear waves that were on contrary to the common understanding in sediment acoustics application whereby shear phenomenon are caused by friction between grains [25]. It was understood that the shear wave speed is much smaller than compression wave speed and even sound speed in majority of the marine sediment's type. In Figure 4.10(b) was also observed to be much smaller than the effects we observed in compression waves in Section 4.1.1. Henceforth, our simulation model could be useful for future studies for shear waves phenomenon in a granular channel. Future studies can include the frictional forces between grain and analyzed both sets of results to provide a more comprehensive explanation for the results shown in below plot. A comparison of results can be done with that of one that include friction parameter within our simulation model in LAMMPs.

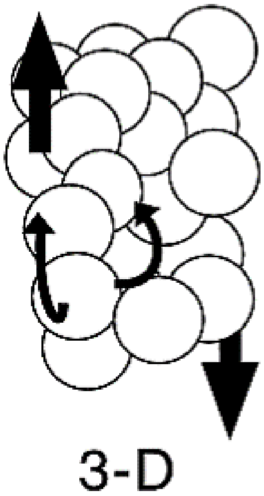

Figure 4.9. Schematics of 3D force components due to shear from a laboratory experiment. Adapted from [26].

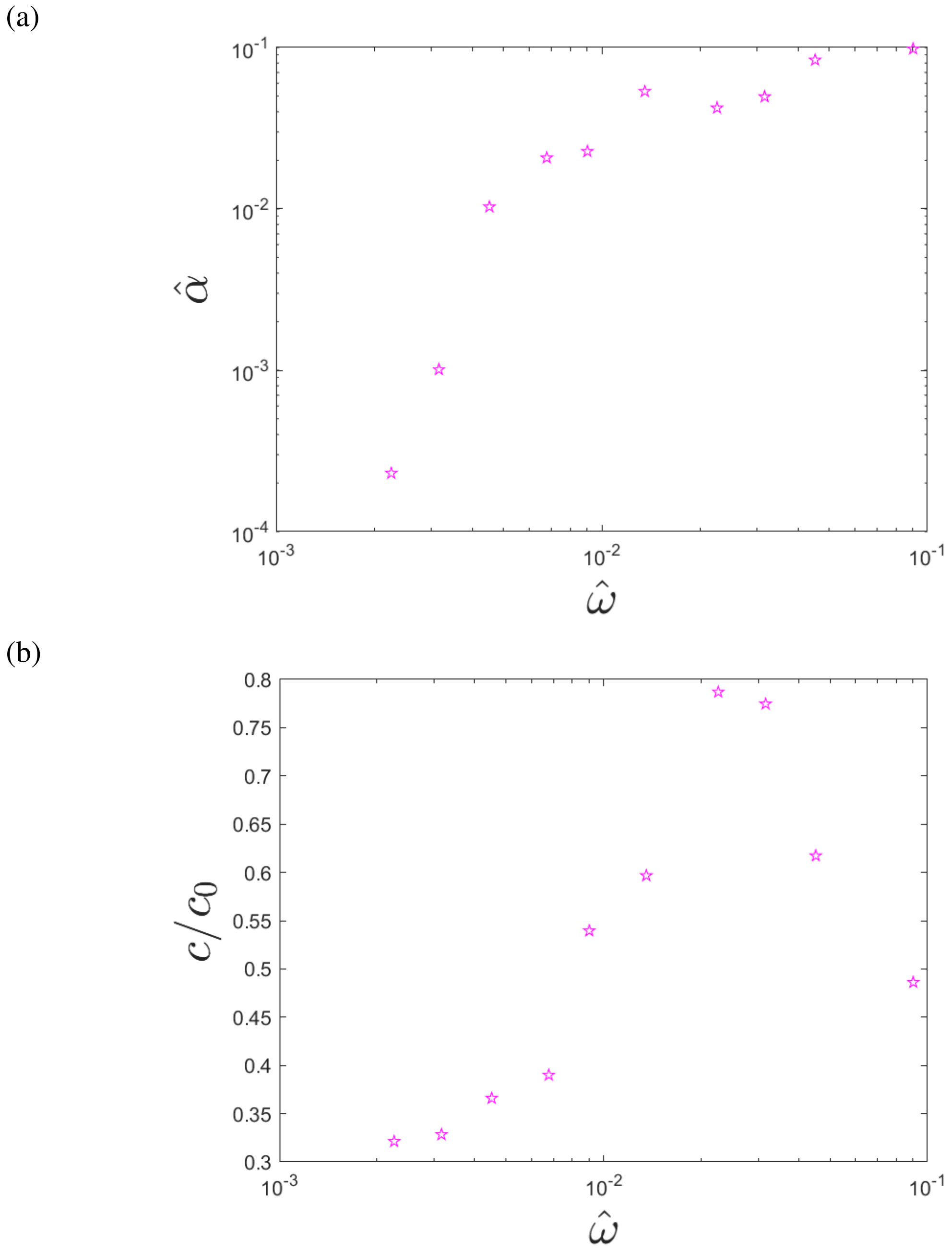

Figure 4.10. Shear effects in z direction at high frequency, $f = 1$

4.4 Effect of Restitution Coefficient

In chapter 2.1.2, we explained the different forms of energy dissipation from normal contacts and that our dashpot term was designed to model some combination of these effects. In this section, we explicitly vary the value of the dashpot term by the physical parameter restitution coefficient, e_n and analyze its effects on dispersion relation. A different e_n value will correspond to a different value for our dashpot term, γ as shown in Table 4.1. We note that setting the dashpot magnitude in this way assumes that the relevant physics are purely from effects that would be seen in dry granular media, and the fluid is playing no role.

Table 4.1. Value of γ with different e_n

e_n	γ
0.2	32
0.5	14
0.9	2.14

In Figure 4.11, we observed no significant variances across the three different e_n value, corresponding to value of γ, for both frequency dependence attenuation and sound speed dispersion. We observe the correct functional form of dispersion relation in our simulation for different γ values. The attenuation coefficients tend to increase with increasing dashpot magnitudes. However, they do not increase as fast as the 1D theory would predict, so future work is needed.

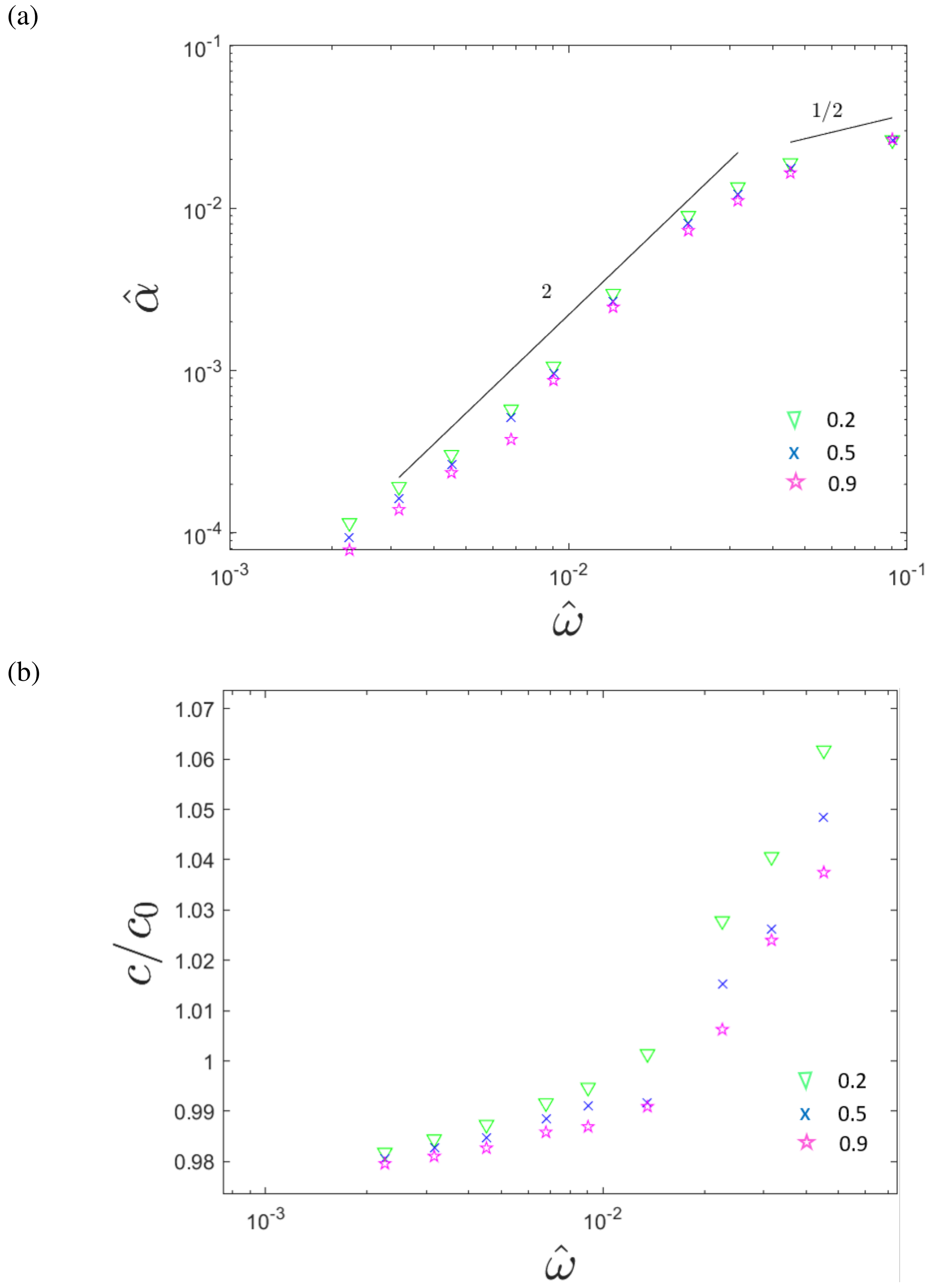

Figure 4.11. (a) attenuation coefficient, $\hat{\alpha}$, and (b) sound speed ratio, c/c_0 for different e_n value.

CHAPTER 5:
Conclusion

This paper presents a granular-based simulation model to study dispersion relations in sediments, where the energy loss occurs purely during normal compression at grain-grain contacts. This loss is modeled via a dashpot term for normal compression. This dashpot term was meant to capture multiple different dissipative effects, including grain-grain restitution as well as possibly an enhancement due to viscous forces as grains move relative to one another. We treated the magnitude of the dashpot as a frequency-independent constant, meaning that the frequency dependence that was observed arises is fundamentally related to a competition between wavelength and grain size. To the extent that viscous forces are needed to match the dashpot value with the experimental data, then this approach bears some resemblance to Biot-Stoll theory. However, we emphasize that our approach is fundamentally granular, meaning that we simply solve a large number of coupled ordinary differential equations for grains in a disordered packing, while Biot-Stoll theory is a fundamentally continuum model that does not include the inherent disorder and heterogeneity of granular media. We demonstrated that even in disordered granular packing, with persistent inter-particles contacts, our simulations produce the correct functional form of the dispersion relations observed in experimental data. This re-affirmed the merits of considering sediment acoustics as a granular mechanics problem.

First, we demonstrated that an unexplored loss mechanism, termed as compression losses, has substantial effects on the dispersion relation. Despite it being a well-established loss mechanism with decades of theoretical and experimental study, this loss mechanism has not been explicitly included in existing theories of sediment acoustics. In our simulation, compression waves were introduced into the channel and its corresponding effects on inter-particles interactions were measured. We observed that $\hat{\alpha}$ showed striking agreement with our 1D theory over the range of frequency used in our simulations, showing $\hat{\alpha}$ proportional to f^2 at low frequency range and $f^{\frac{1}{2}}$ at high frequency range. Sound speed ratio also appeared constant at lower frequency and grew at high frequencies, but in better agreement with the experimental data than the 1D theory, where the sound speed grew without bound according to power law in frequency at high frequencies. Overall, these results generally support our hypothesis that the dominant loss mechanism may be losses at grain-grain compressions. This motivates further studies and development of 3D theory to strengthen our hypothesis holistically.

Next, we examined the practicality of our DEM simulation method for modelling quasi-infinite system. To do so, we ran our simulations with different channel lengths that were controlled by the width (W) of the channel and compared their results. The 3 different channel width followed the same scaling behavior (See Figure 4.5) as our experimental data suggesting that we have reached the large system limits. Despite having similar scaling behavior, we observed that $W = 7$, corresponding to shortest channel length, tend to be more sensitive and least reliable, with large variations between each frequency. This demonstrates that finite channels can be used, but with caution when wavelength becomes similar to channel dimension.

Lastly, we studied the effect of shear waves on our simulation model by oscillating the lower boundary wall in the transverse direction and its effect on attenuation and sound speed dispersion. We analyzed the shear waves phenomenon on our channel without including frictional forces in grain-grain interactions within our simulation. Interestingly, shear waves appeared to behave similarly to compression waves despite a lack of friction between grains. This highlights the fact that shear rigidity exists even in frictionless granular packing. The non-linearity in z displacement observed in Figure 4.6 were a result of irregularly packing arrangement of granular in the channel that affects the inter-particle interactions and its resultant force components. Our results suggest that the packing method and its associated packing arrangement may have an impact when studying the attenuation and sound speed dispersion effects, especially for shear waves.

Our preliminary results were a ‘dipstick’ test of the validity of our hypothesis on our 1D theory that compression losses alone count account for the rate of attenuation observed from experimental data collected from different sites with different seabed bottom. More simulations could be done to study the effect of poly-dispersity and expand the range of current simulation parameters used in this paper. Future research works should continue to develop the 3D theory and validate them using existing discrete element simulations, thereafter comparing both sets of results with experimental data. To bring the work further and its application in sediment acoustics, simulations works should also analyze the effects of fluid viscosity to sound speed and attenuation using Stokes-like drag terms. In addition, the effects of physical mechanisms within the grains in the high frequency limits.

In conclusion, we had developed a discrete element simulation method and validated compression losses as the dominant loss mechanism using our 1D theory. This approach simplified sediment acoustics propagation theory by reducing the number of material fit parameters required to predict sediment acoustics, focusing on material fit parameters that are explicitly rooted to their granular nature, namely k, d, and γ. These parameters unlike those used in most theories, where values of the parameters can only be known on physical sites, are measurable from core samples in laboratory and accurately estimated in most instances. Operationally, this provides war-fighter better pre-operation analysis and removes operational uncertainty on the ground that improves overall operational effectiveness. Henceforth, the small number of fit parameters coupled with a relatively simple theory, which were already well established in the granular physics field, can present a more tractable problem for geo-acoustics inversion that will possibly be an enabler for better target detection system and remote sensing capabilities in the undersea realm.

THIS PAGE INTENTIONALLY LEFT BLANK

APPENDIX A:
MATLAB Code(Generate Particles)

```
function MakeLammpsICs(N,W)
%% Set Input Parameters %%%%%%%%%%%%%%%%%%%%%%%%%
% N=1000;
varsname=['N' num2str(N) 'W' num2str(W)];
% Names of files
filename=['./LAMMPS_files/data_IC' varsname '.granular'];
% Average Particle size in Simulation Units
d_ave=1;
% Density of particles
rho=1;
%% Calculate Values Needed for Text File
% Size and density of wall particles
    rho_wall=0.05*rho;
    d_max=1.3*d_ave;
    d_wall=2*d_ave;
% Calculate Width of Box in Simulation Units
    Wbox=ceil(W.*d_ave);
% Wall particle position vectors
% All wall particles are d_max
    sq_wall_pos=[d_max/2:d_max:ceil(W*d_ave)];
    all_x_wall=ones(length(sq_wall_pos),1)*sq_wall_pos;
    all_x_wall=all_x_wall(:)'-(W*d_ave)/2;
%      all_x_wall=[all_x_wall,all_x_wall+0.3*d_max,all_x_wall
   -0.3*d_max];

    all_y_wall=(ones(length(sq_wall_pos),1)*sq_wall_pos)';
    all_y_wall=all_y_wall(:)'-(W*d_ave)/2;
%      all_y_wall=[all_y_wall,all_y_wall+0.3*d_max,all_y_wall
   -0.3*d_max];
```

```
% Calculate number of particles in tightly packed walls
% Nlower=ceil((Wbox/d_max).^2);
% Nupper=ceil((Wbox/d_max).^2);
    Nlower=length(all_y_wall);
    Nupper=Nlower;

    Ntot=N+Nlower+Nupper;

% Flow particles per layer
    sq_flow=[(1.5*d_ave):(1.5*d_ave):Wbox];

%Placement of flow particles
    layer_x_flow=ones(length(sq_flow),1)*sq_flow;
    layer_x_flow=layer_x_flow(:)'-(W*d_ave)/2;

    layer_y_flow=(ones(length(sq_flow),1)*sq_flow)';
    layer_y_flow=layer_y_flow(:)'-(W*d_ave)/2;

% Approxmate number of flow layers needed
    FlowLayers=ceil(N/length(layer_y_flow));

% Set Height of Box
    %Hbox=(10*d_max)+ceil(N./((W/3.2).^2))*3;
    Hbox=(7*d_max)+(3*(FlowLayers+2)*d_ave);

% Raise and lower all particles within 0.5 grain diameters
   to create
% roughness on walls
    add_lower=0.2*randn(1,Nlower);
    add_upper=0.2*randn(1,Nupper);

    z_wall_upper_pos=Hbox-2.5*d_max+add_upper;%[Hbox-2.5*
```

```
       d_max+add_upper,Hbox-d_max+zeros(1,(Nupper/3)),Hbox
       -1.5*d_max+zeros(1,(Nupper/3))];
    z_wall_lower_pos=add_lower+1*d_max;%[add_lower+1*d_max,
       zeros(1,Nlower/3),zeros(1,Nlower/3)-0.5*d_max];
    %z_wall_upper_pos=[Hbox-2.5*d_max+add_upper,Hbox-1.5*
       d_max+add_upper,Hbox-0.5*d_max+add_upper];

% Set Positions for all flow particles
    sq_flow_h=[(2*d_max):(1*d_ave):(Hbox-2*d_max)];

    all_z_flow=ones(length(layer_x_flow),1)*sq_flow_h;
    all_z_flow=all_z_flow(:)';
    all_z_flow = all_z_flow + 0*(rand(size(all_z_flow))-0.5)
       ;

    all_x_flow=(ones(length(sq_flow_h),1)*layer_x_flow)';
    all_x_flow=all_x_flow(:)';
    all_x_flow = all_x_flow + 0.5*(rand(size(all_z_flow))
       -0.5);

    all_y_flow=(ones(length(sq_flow_h),1)*layer_y_flow)';
    all_y_flow=all_y_flow(:)';
    all_y_flow = all_y_flow + 0.5*(rand(size(all_z_flow))
       -0.5);

    % Move wall down

    z_wall_upper_pos = z_wall_upper_pos + 2 - (min(
       z_wall_upper_pos)-max(all_z_flow(1:N)));

%% Make Text File %%%%%%%%%%%%%%%%%%%%%%%%%%%%%%%%

fileID=fopen(filename,'w');
```

```
fprintf(fileID,['LAMMPS 3d granular data file\n'
   UU
   ...
    '\n'...
    num2str(Ntot) ' atoms\n'...
    '0 bonds\n'...
    '0 angles\n'...
    '0 dihedrals\n'...
    '0 impropers\n'...
    '\n'...
    '3 atom types\n'...
    '0 bond types\n'...
    '0 angle types\n'...
    '0 dihedral types\n'...
    '0 improper types\n'...
    '\n'...
    num2str(-Wbox/2) ' ' num2str(Wbox/2) ' xlo xhi\n'...
    num2str(-Wbox/2) ' ' num2str(Wbox/2) ' ylo yhi\n'...
    num2str(-2*d_ave) ' ' num2str(Hbox) ' zlo zhi\n'...
    '\n'...
    '\n'...
    'Atoms\n'...
    '\n']);

atomID=1:Ntot;
atomtype=[ones(1,Nlower)*2,ones(1,Nupper)*3,ones(1,N)];
diameter=[ones(1,Nlower)*d_wall,ones(1,Nupper)*d_wall,0.2*
   randn(1,N)+d_ave];
rho_all=[ones(1,Nlower)*rho_wall,ones(1,Nupper)*rho_wall,
   ones(1,N)*rho];
x_all=[all_x_wall,all_x_wall,all_x_flow(1:N)];
y_all=[all_y_wall,all_y_wall,all_y_flow(1:N)];
```

```
z_all=[z_wall_lower_pos,z_wall_upper_pos,all_z_flow(1:N)];

Amat = [atomID;atomtype;diameter;rho_all;x_all;y_all;z_all];

%Format is atom_ID, atom_type, diameter, rho, x, y, z
formatSpec = '%.0f %.0f %.3f  %.3f %.4f %.4f %.4f\n';
fprintf(fileID,formatSpec,Amat);
fclose(fileID);
figure,
plot3(x_all,y_all,z_all,'.')
end
```

THIS PAGE INTENTIONALLY LEFT BLANK

APPENDIX B:
LAMMPS Code(Compress Channel)

```
# Pour granular particles into periodic box with a floor,
   then impact

# "Units" definition is meaningless, only dimensionless
   numbers matter
units           si

# AMP and FREQ are now passed in from the function call.
   However, these lines can be
# uncommented and AMP and FREQ can be set directly in the
   script. Physically, these
# correspond to the amplitude and frequency of the applied
   vibration

variable        AMP equal 0
variable        FREQ equal 1.0

variable        PER equal 1/${FREQ}
variable        density equal 1
#variable       E equal 1000     #Young Modulus aka k
   constant
#variable       coeffFric equal 0
#variable       P equal 1

variable        PI equal 3.141592653589
variable        seed equal 1056738

variable Nt equal 30000000     # Number of time steps
```

```
###############################################
# Granular contact parameters

# Everything in this section is set up to calculate kn, kt,
   gamma_n, and gamma_t in terms
# of physically meaningful numbers like the Young's modulus
   and the grain diameter

# However, these parameters can be set directly
###############################################

variable        coeffRes equal 0.2
#variable       coeffFric equal MU

variable        EYoung equal $E
variable        Poisson equal 2.0/7.0
variable        GShear equal ${EYoung}/(2*(1+${Poisson}))
variable        gravity equal 1
variable        reff equal 1
variable        meff equal ${density}*4.0/3.0*${PI}*${reff
   }^3
variable        min_mass equal ${density}*4.0/3.0*${PI
   }*0.064
variable        max_mass equal ${density}*4.0/3.0*${PI
   }*0.216

## Typical way to set kn, kt, etc.:
variable        kn equal 4.0*${GShear}/(3*(1-${Poisson}))
variable        kt equal 4.0*${GShear}/(2-${Poisson})
variable        a equal (-2.0*log(${coeffRes})/${PI})^2
variable        gamma_n equal sqrt($a*2*${kn}/${min_mass
   }/(1+0.25*$a))
variable        gamma_t equal ${gamma_n}*0.5
```

```
variable        tcol equal ${PI}/sqrt(2*${kn}/${min_mass}-${
   gamma_n}/4.0)
variable        dt equal ${tcol}*0.01
timestep        ${dt}

print "dt = ${dt}, period = ${PER}"

###############################################

variable        dumpfreq equal 1000
variable        logfreq equal 1000

atom_style      sphere
boundary        p p s
newton          off
comm_modify     vel yes

########### SIZE OF "SKIN" FOR NEIGHBOR LISTS
   ################
neighbor        0.3 bin

########### TIME STEPS TO DELAY FOR THE N^2 BUILD
   ################
neigh_modify    delay 100 every 100 check yes
neigh_modify    exclude type 2 2
neigh_modify    exclude type 3 3
neigh_modify    exclude type 2 3
#neigh_modify   delay 5

read_data       ./data_ICN$NW$W.granular
read_dump restarts/dump.restart.N$NW$WP$PE$Emu${coeffFric}
   ${Nt_restart} x y z
```

```
group           lower type 2
group           upper type 3
group           flow type 1

pair_style      gran/hooke/history &
                ${kn} ${kt} ${gamma_n} ${gamma_t} ${
                   coeffFric} 1
pair_coeff      * *

###############################################
# Computations for output dumps (needs modification)
###############################################

compute         mobile all erotate/sphere
compute         t1 all temp/sphere
compute         1 flow group/group upper
compute         2 upper group/group flow
compute myPress flow stress/atom NULL virial
compute 4 upper group/group flow
compute 5 all temp

variable vdw equal c_1
variable fx equal c_1[1]
variable fy equal c_1[2]
variable fz equal c_1[3]
variable time equal step*dt

variable f1 equal c_4[1]
variable f2 equal c_4[2]
variable f3 equal c_4[3]

variable sigma_xx equal c_3[1]
variable sigma_yy equal c_3[2]
```

```
variable sigma_zz equal c_3[3]
variable sigma_xy equal c_3[4]
variable sigma_xz equal c_3[5]
variable sigma_yz equal c_3[6]

fix 7 all print 1000 "${time} ${f1} ${f2} ${f3}" file
   output_SedAcoust/output_N$N_f${FREQ}_A${AMP}_mu${
   coeffFric}_E${EYoung}_P$P.txt screen "no" title "#time fx
    fy fz"

fix             1 flow nve/sphere

fix             3 upper move linear 0.0 0.0 NULL
fix                     4 upper aveforce 0.0 0.0 -$P
fix             6 lower move wiggle 0 0 0 ${PER}
fix 8 all viscous 0.01
 thermo_style   custom step atoms ke vol
 thermo         1000
 thermo_modify  temp t1
 thermo_modify  lost ignore norm no
 compute_modify thermo_temp dynamic/dof yes

dump 4a all atom 1000000 restarts/dump.restart.N$NW$WP$PE$
   Emu${coeffFric}

variable myTemp equal temp
label loop
variable Loop_Count loop 10000
run 10000
if "${myTemp} < 100000" then "jump SELF break"
next Loop_Count
jump SELF loop
label break
```

```
print "ALL DONE"

write_restart restarts/restart.N$NW$WP$PE$Emu${coeffFric}
dump_modify 4a every 2
dump_modify 4a format line "%d %d %3.16f %3.16f %3.16f"
   scale yes

run 1
```

APPENDIX C:
LAMMPS Code(Generate Waves)

```
variable        PER equal 1/${FREQ}
variable        density equal 1
variable        PI equal 3.141592653589
variable        seed equal 1056738

variable Nt equal 900000   # Number of time steps

###############################################
# Granular contact parameters

# Everything in this section is set up to calculate kn, kt,
   gamma_n, and gamma_t in terms
# of physically meaningful numbers like the Young's modulus
   and the grain diameter

# However, these parameters can be set directly
###############################################

#variable       coeffRes equal 0.2
#variable       coeffFric equal MU

variable        EYoung equal $E
variable        Poisson equal 2.0/7.0
variable        GShear equal ${EYoung}/(2*(1+${Poisson}))
variable        gravity equal 1
variable        reff equal 1
variable        meff equal ${density}*4.0/3.0*${PI}*${reff
   }^3
variable        min_mass equal ${density}*4.0/3.0*${PI
```

```
   }*0.064
variable        max_mass equal ${density}*4.0/3.0*${PI
   }*0.216

## Typical way to set kn, kt, etc.:
variable        kn equal 4.0*${GShear}/(3*(1-${Poisson}))
variable        kt equal 4.0*${GShear}/(2-${Poisson})
variable        a equal (-2.0*log(${coeffRes})/${PI})^2
variable        gamma_n equal sqrt($a*2*${kn}/${min_mass
   }/(1+0.25*$a))
variable        gamma_t equal ${gamma_n}*0
variable        tcol equal ${PI}/sqrt(2*${kn}/${min_mass}-${
   gamma_n}/4.0)
variable        dt equal ${tcol}*0.01
timestep        ${dt}

print "dt = ${dt}, period = ${PER}"
print "kn = ${kn}, gamma_n = ${gamma_n}, gamma_t = ${gamma_t
   }"

###############################################

variable        dumpfreq equal 1000
variable        logfreq equal 1000

atom_style      sphere
boundary        p p s
newton          off
comm_modify     vel yes

########### SIZE OF "SKIN" FOR NEIGHBOR LISTS
   ################
neighbor        0.1 bin
```

```
########### TIME STEPS TO DELAY FOR THE N^2 BUILD
   ################
neigh_modify    delay 1 every 1 check yes
neigh_modify    exclude type 2 2
neigh_modify    exclude type 3 3
neigh_modify    exclude type 2 3
#neigh_modify   delay 5

# variable Nt_restart equal 1430000
read_data       ./data_ICN$NW$W.granular
read_dump restarts_done/dump.restart.N$NW$WP$PE$Emu${
   coeffFric} ${Nt_restart} x y z

group           lower type 2
group           upper type 3
group           flow type 1

group       measure id 100 200 300 400 500
compute 800 measure property/atom x y z
dump 4a measure custom 5 output_W5/output_N$N_f${FREQ}_en${
   coeffRes}_A${AMP}_mu${coeffFric}_E${EYoung}_P$P.txt id z
   fz
dump_modify 4a format float  %3.6f

pair_style      gran/hooke/history &
                ${kn} ${kt} ${gamma_n} ${gamma_t} ${
                   coeffFric} 1
pair_coeff      * *

print "kn = ${kn}, gamma_n = ${gamma_n}"

###############################################
```

```
# Computations for output dumps (needs modification)
###############################################

compute         mobile all erotate/sphere
compute         t1 all temp/sphere
compute         1 flow group/group upper
compute         2 upper group/group flow
compute myPress flow stress/atom NULL virial
#compute 3 flow reduce ave c_myPress[*]
compute 4 upper group/group flow
compute 5 all temp

variable vdw equal c_1
variable fx equal c_1[1]
variable fy equal c_1[2]
variable fz equal c_1[3]
variable time equal step*dt

variable f1 equal c_4[1]
variable f2 equal c_4[2]
variable f3 equal c_4[3]

variable z1 equal "x[101]"


variable sigma_xx equal c_3[1]
variable sigma_yy equal c_3[2]
variable sigma_zz equal c_3[3]
variable sigma_xy equal c_3[4]
variable sigma_xz equal c_3[5]
variable sigma_yz equal c_3[6]

fix             1 flow nve/sphere
```

```
fix         3 upper freeze

fix             6 lower move wiggle 0 0 ${AMP} ${PER} (
   Longitudinal)
fix             6 lower move wiggle ${AMP} 0 0  ${PER} (
   Transverse)

 thermo_style   custom step atoms ke vol
 thermo         1000
 thermo_modify  temp t1
 thermo_modify  lost ignore norm no
 compute_modify thermo_temp dynamic/dof yes

testimages/image.${N}.${EYoung}.${coeffFric}.${seed}.*.jpg
   type type &
                center d 0.5 0.5 0.5 axes yes 0.8 0.02 view
                   80 -30 size 1000 1000 zoom 1

run ${Nt}
```

THIS PAGE INTENTIONALLY LEFT BLANK

List of References

[1] R. J. Urick, *Principles of underwater sound-2*. New York, NY (USA) McGraw-Hill Book, 1975.

[2] D. Jackson and M. Richardson, *High-frequency seafloor acoustics*. Springer Science & Business Media, 2007.

[3] J.-X. Zhou, X.-Z. Zhang, and D. Knobles, "Low-frequency geoacoustic model for the effective properties of sandy seabottoms," *The journal of the acoustical society of America*, vol. 125, no. 5, pp. 2847–2866, 2009.

[4] N. P. Chotiros, "Biot model of sound propagation in water-saturated sand," *The Journal of the Acoustical Society of America*, vol. 97, no. 1, pp. 199–214, 1995.

[5] R. D. Stoll *et al.*, *Sediment Acoustics*. Springer, 1989, vol. 26.

[6] M. A. Biot, "Theory of propagation of elastic waves in a fluid-saturated porous solid. II. higher frequency range," *The Journal of the Acoustical Society of America*, vol. 28, no. 2, pp. 179–191, 1956.

[7] M. J. Buckingham, "Theory of acoustic attenuation, dispersion, and pulse propagation in unconsolidated granular materials including marine sediments," *The Journal of the Acoustical Society of America*, vol. 102, no. 5, pp. 2579–2596, 1997.

[8] M. J. Buckingham, "Wave speed and attenuation profiles in a stratified marine sediment: Geo-acoustic modeling of seabed layering using the viscous grain shearing theory," *The Journal of the Acoustical Society of America*, vol. 148, no. 2, pp. 962–974, 2020.

[9] M. J. Buckingham, "On pore-fluid viscosity and the wave properties of saturated granular materials including marine sediments," *The Journal of the Acoustical Society of America*, vol. 122, no. 3, pp. 1486–1501, 2007.

[10] N. P. Chotiros and M. J. Isakson, "A broadband model of sandy ocean sediments: Biot–stoll with contact squirt flow and shear drag," *The Journal of the Acoustical Society of America*, vol. 116, no. 4, pp. 2011–2022, 2004.

[11] N. P. Chotiros and M. J. Isakson, "High-frequency dispersion from viscous drag at the grain-grain contact in water-saturated sand," *The Journal of the Acoustical Society of America*, vol. 124, no. 5, pp. EL296–EL301, 2008.

[12] M. J. Buckingham, “Wave propagation, stress relaxation, and grain-to-grain shearing in saturated, unconsolidated marine sediments,” *The Journal of the Acoustical Society of America*, vol. 108, no. 6, pp. 2796–2815, 2000.

[13] A. H. Clark, L. Kondic, and R. P. Behringer, “Particle scale dynamics in granular impact,” *Physical Review Letters*, vol. 109, no. 23, p. 238302, 2012.

[14] N. Krizou and A. H. Clark, “Power-law scaling of early-stage forces during granular impact,” *Physical Review Letters*, vol. 124, no. 17, p. 178002, 2020.

[15] T. Pähtz, A. H. Clark, M. Valyrakis, and O. Durán, “The physics of sediment transport initiation, cessation, and entrainment across aeolian and fluvial environments,” *Reviews of Geophysics*, vol. 58, no. 1, p. e2019RG000679, 2020.

[16] J. Shäfer, S. Dippel, and D. Wolf, “Force schemes in simulations of granular materials,” *Journal de physique I*, vol. 6, no. 1, pp. 5–20, 1996.

[17] P. A. Cundall and O. D. Strack, “A discrete numerical model for granular assemblies,” *Geotechnique*, vol. 29, no. 1, pp. 47–65, 1979.

[18] F. Di Puccio and L. Mattei, “Biotribology of artificial hip joints,” *World Journal of Orthopedics*, vol. 6, no. 1, p. 77, 2015.

[19] S. Timoshenko, *History of strength of materials: With a brief account of the history of theory of elasticity and theory of structures*. Courier Corporation, 1983.

[20] C. Coste and B. Gilles, “On the validity of Hertz contact law for granular material acoustics,” *The European Physical Journal B-Condensed Matter and Complex Systems*, vol. 7, no. 1, pp. 155–168, 1999.

[21] A. Maccabi, A. Shin, N. K. Namiri, N. Bajwa, M. St. John, Z. D. Taylor, W. Grundfest, and G. N. Saddik, “Quantitative characterization of viscoelastic behavior in tissue-mimicking phantoms and ex vivo animal tissues,” *PloS one*, vol. 13, no. 1, p. e0191919, 2018.

[22] A. P. Thompson, H. M. Aktulga, R. Berger, D. S. Bolintineanu, W. M. Brown, P. S. Crozier, P. J. in’t Veld, A. Kohlmeyer, S. G. Moore, T. D. Nguyen *et al.*, “LAMMPS-a flexible simulation tool for particle-based materials modeling at the atomic, meso, and continuum scales,” *Computer Physics Communications*, vol. 271, p. 108171, 2022.

[23] Y.-M. Jiang and N. R. Chapman, “Measurement of low-frequency sound attenuation in marine sediment,” *IEEE Journal of Oceanic Engineering*, vol. 35, no. 1, pp. 70–78, 2010.

[24] H. Zhu, Y. Wu, and A. Yu, “Discrete and continuum modelling of granular flow,” *China Particuology*, vol. 3, no. 6, pp. 354–363, 2005.

[25] K. Mair, K. M. Frye, and C. Marone, “Influence of grain characteristics on the friction of granular shear zones,” *Journal of Geophysical Research: Solid Earth*, vol. 107, no. B10, pp. ECV–4, 2002.

[26] K. M. Frye and C. Marone, “The effect of particle dimensionality on granular friction in laboratory shear zones,” *Geophysical Research Letters*, vol. 29, no. 19, pp. 22–1, 2002.

THIS PAGE INTENTIONALLY LEFT BLANK

Initial Distribution List

1. Defense Technical Information Center
   Ft. Belvoir, Virginia

2. Dudley Knox Library
   Naval Postgraduate School
   Monterey, California